Global Biogeochemical Cycles

RESEARCH ARTICLE
10.1029/2020GB006674

Trace Element Biogeochemistry in the High-Latitude North Atlantic Ocean: Seasonal Variations and Volcanic Inputs

Eric P. Achterberg[1,2], Sebastian Steigenberger[1,3], Jessica K. Klar[4], Thomas J. Browning[2], Chris M. Marsay[5], Stuart C. Painter[3], Lúcia H. Vieira[2], Alex R. Baker[6], Douglas S. Hamilton[7], Toste Tanhua[2], and C. Mark Moore[1]

[1]Ocean and Earth Science, National Oceanography Centre Southampton, University of Southampton, Southampton, UK, [2]GEOMAR Helmholtz Centre for Ocean Research Kiel, Kiel, Germany, [3]National Oceanography Centre, Southampton, UK, [4]Centre de Formation et de Recherche sur les Environnements Méditerranéens (CEFREM), UMR 5110, Université de Perpignan Via Domitia, CNRS, Perpignan, France, [5]Skidaway Institute of Oceanography, University of Georgia, Savannah, GA, USA, [6]School of Environmental Sciences, University of East Anglia, Norwich, UK, [7]Department of Earth and Atmospheric Science, Cornell University, Ithaca, NY, USA

Key Points:
- Bio-essential element concentrations in surface waters decreased from spring to summer with removal ratios reflecting biological uptake
- Effects of volcanic inputs from Eyjafjallajökull in spring 2010 were pronounced for Al, Mn, and Zn but returned to typical levels in summer
- Deep winter convection dominated trace element supply to surface waters with minor contributions from atmospheric and diffusive mixing

Supporting Information:
- Supporting Information S1

Correspondence to:
E. P. Achterberg,
eachterberg@geomar.de

Citation:
Achterberg, E. P., Steigenberger, S., Klar, J. K., Browning, T. J., Marsay, C. M., Painter, S. C., et al. (2021). Trace element biogeochemistry in the high-latitude North Atlantic Ocean: Seasonal variations and volcanic inputs. *Global Biogeochemical Cycles*, *34*, e2020GB006674. https://doi.org/10.1029/2020GB006674

Received 18 MAY 2020
Accepted 13 NOV 2020
Accepted article online 25 NOV 2020

Abstract We present dissolved and total dissolvable trace elements for spring and summer cruises in 2010 in the high-latitude North Atlantic. Surface and full depth data are provided for Al, Cd, Co, Cu, Mn, Ni, Pb, and Zn in the Iceland and Irminger Basins, and consequences of biological uptake and inputs by the spring Eyjafjallajökull volcanic eruption are assessed. Ash from Eyjafjallajökull resulted in pronounced increases in Al, Mn, and Zn in surface waters in close proximity to Iceland during the eruption, while 3 months later during the summer cruise levels had returned to more typical values for the region. The apparent seasonal removal ratios of surface trace elements were consistent with biological export. Assessment of supply of trace elements to the surface mixed layer for the region, excluding volcanic inputs, indicated that deep winter mixing was the dominant source, with diffusive mixing being a minor source (between 13.5% [dissolved Cd, DCd] and −2.43% [DZn] of deep winter flux), and atmospheric inputs being an important source only for DAl and DZn (DAl up to 42% and DZn up to 4.2% of deep winter + diffusive fluxes) and typically less than 1% for the other elements. Elemental supply ratios to the surface mixed layer through convection were comparable to apparent removal ratios we calculated between spring and summer. Given that deep mixing dominated nutrient and trace element supply to surface waters, predicted increases in water column stratification in this region may reduce supply, with potential consequences for primary production and the biological carbon pump.

1. Introduction

Primary productivity, standing stock, species composition, and trophic structure of planktonic communities in the oceans are controlled by the availability of light, macronutrients (nitrogen [N], phosphorus [P], and silicon [Si]) and the micronutrient iron (Fe), in association with loss processes by viral lysis and zooplankton grazing (Boyd et al., 2007; Graziano et al., 1996; Martin, 1991; Nelson et al., 2001; Wu et al., 2000). These controls influence export production and thereby impact the global carbon cycle (Brix et al., 2006). Trace elements other than Fe also play an important role in the functioning of microbial organisms, with the next most abundant trace elements in marine phytoplankton after Fe being (in order) zinc (Zn), manganese (Mn), copper (Cu), nickel (Ni), cadmium (Cd), and cobalt (Co) (Twining & Baines, 2013).

These micronutrient trace metals play key roles in a range of cellular processes that ultimately determine rates of oceanic primary productivity (Morel & Price, 2003). The availability of these micronutrient elements can therefore influence the fixation of CO_2, generation of O_2, uptake of N, P, and Fe, with enhanced levels potentially resulting in toxic effects (Morel & Price, 2003). The involvement in biological processes results in a removal of micronutrients like Cd, Cu, Ni, and Zn from the surface ocean by microbial organisms, with release at depth following remineralization of sinking particles (Bruland & Lohan, 2004).

The supply and removal processes of the oceanic micronutrients can be elucidated with the use of tracers, such as aluminum (Al) for dust inputs (Vink & Measures, 2000), Mn for benthic supply (Laès et al., 2007),

and lead (Pb) for scavenging (Kadko, 1993). We still have a limited understanding of the oceanic distributions and cycling of trace elements, despite their important biogeochemical roles. In recent years, large new data sets have emerged as part of the international GEOTRACES program (Henderson et al., 2007; Schlitzer et al., 2018). The availability of oceanic Fe data has substantially improved (e.g., Fitzsimmons et al., 2017; Milne et al., 2017; Tagliabue et al., 2012), with also some new data sets for, for example, Zn (Middag et al., 2019; Wyatt et al., 2014), Al (Measures et al., 2015; Menzel Barraqueta et al., 2018), Pb (Noble et al., 2015; Rusiecka et al., 2018), Cd (Middag et al., 2018; Wu & Roshan, 2015), and Ni (Middag et al., 2020).

The high-latitude North Atlantic Ocean features a pronounced annual spring bloom (Sanders et al., 2005) and has areas of deep water formation, and therefore forms an important component of the oceanic carbon cycle (Broecker, 1991; Pickart et al., 2003). The typical annual phytoplankton bloom in the high-latitude North Atlantic starts in early April and lasts toward mid-May, with a second peak toward the end of June, followed by chlorophyll a levels decreasing afterward (Achterberg et al., 2013; Sanders et al., 2005). The region has become a focus for research into the role of Fe in ocean productivity, community structure and carbon export (Browning et al., 2019; Giering et al., 2012; Le Moigne et al., 2014; Moore et al., 2006; Nielsdottir et al., 2009; Ryan-Keogh et al., 2013). Residual nitrate concentrations have been observed during late spring and summer in surface waters of the high-latitude North Atlantic (Moore et al., 2006; Nielsdottir et al., 2009), indicating a reduced efficiency of the biological carbon pump (Sarmiento & Toggweiler, 1984). Limitation of phytoplankton growth, resulting in the residual nitrate levels, has been attributed to a limited supply and availability of Fe (Achterberg et al., 2013, 2018; Nielsdottir et al., 2009; Ryan-Keogh et al., 2013).

This study is part of the Irminger Basin Iron Study (IBIS) and presents the distributions of dissolved and total dissolvable Al, Cd, Cu, Mn, Ni, Pb, and Zn, and the quantification of their various sources to and removal mechanisms from the surface ocean of the high-latitude North Atlantic. The geographical focus of IBIS was the Iceland Basin (IB) and Irminger Basin (IRB). Research cruises in different seasons (spring and summer) as part of IBIS were conducted during and after an eruption of the Eyjafjallajökull volcano which impacted the study region (Achterberg et al., 2013). The study therefore allowed for a unique seasonal perspective of the effects of trace element cycling in the study region, including a direct assessment of volcanic inputs, for which some indirect but few direct observations exist (e.g., Duggen et al., 2007; Hamme et al., 2010; Lin et al., 2011). A recent paper has reported on the distributions of dissolved and dissolvable Fe in the study region as part of IBIS Programme (Achterberg et al., 2018). Here we present multiple elements other than Fe, providing a thorough comparison of their biogeochemical cycles in this study region.

2. Materials and Methods

2.1. Sample Collection

Water samples were obtained in the high-latitude North Atlantic at 41 full depth conductivity, temperature, and depth (CTD) casts and 195 underway surface stations during cruises D350, D351, and D354 on board RRS *Discovery*. The cruises took place in spring and summer 2010 (spring: 26 April to 9 May [D350] and 10–28 May [D351]; summer: 4 July to 11 August [D354]) (cruise tracks in supporting information [SI] Figure S1). The samples were collected in the shelf regions off Iceland (D350, D351, and D354) and Greenland (D354), and in the IB (D350, D351, and D354) and IRB (D350 and D354) (Figure 1). The spring cruises D350 and D351 were conducted during the explosive eruption phase of the Eyjafjallajökull volcano, and the summer cruise sailed following the eruption (Achterberg et al., 2013). All data are available from the British Oceanographic Data Centre.

Samples were collected using trace metal clean 10 L OTE (Ocean Test Equipment) Niskin samplers mounted on a Ti CTD rosette frame. The OTE bottles were immediately transferred into a pressurized clean container (class 1,000) for sub-sampling. In addition, surface seawater (~3 m depth) was pumped from a tow fish into the clean container using a Teflon diaphragm pump (Almatec A15) connected to a clean oil-free air compressor (JunAir) (Achterberg et al., 2001) and samples taken every 2 hr while the ship was in transit.

Samples for trace metal analysis were collected in acid-cleaned 125 or 250 ml low-density polyethylene bottles (LDPE, Nalgene) after on-line filtration with a 0.2 μm cartridge filter (with 0.45 μm pre-filter, Sartobran 300, Sartorius). The samples from the OTE bottles were filtered under pure N_2 pressure

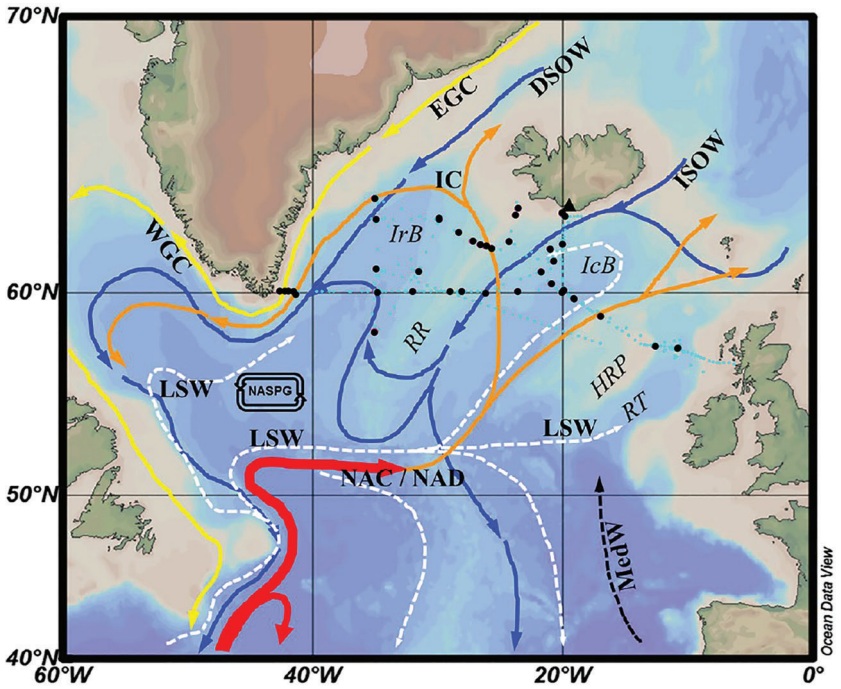

Figure 1. Circulation in the North Atlantic, redrawn from graph originally from IFM-GEOMAR SFB460 overlaid with sampling stations of cruises D350, D351, and D354 (black: CTD, cyan: underway) and the location of the volcano Eyjafjallajökull (black triangle). Red, orange, and yellow: near-surface currents. Dashed black and white: intermediate currents. Blue: near-bottom currents. Abbreviations are LSW: Labrador Sea Water; NAC/NAD: North Atlantic Current/Drift; ISOW: Iceland-Scotland Overflow Water; DSOW: Denmark Strait Overflow Water; NASPG: North Atlantic Sub-Polar Gyre; RT: Rockall Trough; HRP: Hatton-Rockall Plateau; IC: Irminger Current; RR: Reykjanes Ridge; IrB: Irminger Basin; and IcB: Iceland Basin. Map was produced using Ocean Data View (Schlitzer, R., Ocean Data View, odv.awi.de, 2017).

(filtered 99.99% N_2, 1 bar), whereas those from the tow fish were filtered using the pressure from the Teflon pump. Additional samples were collected without filtration. Each sample was acidified to pH ~ 1.9 on board in a laminar flow hood (class 100) with nitric acid (UpA HNO_3, Romil, UK) and stored in double bags until analysis at the National Oceanography Centre Southampton. The storage of the acidified (pH ~ 1.9) unfiltered samples with subsequent analysis after 18 months yielded total dissolvable metal (TDAl, TDCd, TDCo, TDCu, TDMn, TDNi, TDPb, and TDZn) concentrations, which include the dissolved (0.2 μm filtered) and an acid leachable fraction of the particulate pool (no TDAl data available for tow fish surface samples). In order to verify that sampling and sample handling procedures were trace metal clean, samples were analyzed for dissolved Fe (DFe) at sea using a flow injection technique (Obata et al., 1993).

2.2. Trace Metal and Nutrient Analysis

Concentrations of trace metals were determined by isotope dilution inductively coupled mass spectrometry (ID-ICP-MS), while the mono-isotopic elements Co and Mn were analyzed using a standard addition approach followed by ICP-MS detection; all according to methods described in (Rapp et al., 2017). Full details are supplied in the SI (Text S1). The values determined using the ICP-MS method showed good consistency with the reported consensus values for the elements (SI, Table S1). Aluminum in seawater was determined using a flow injection lumogallion method with fluorescence detection (Brown & Bruland, 2008); full details in SI (Text S1). Nitrate + nitrite (Total Oxidized Nitrogen: TON), silicic acid and phosphate were analyzed at sea using standard auto-analyzer techniques (Grasshoff et al., 1983) on a Skalar instrument, following the best practice guide for performing nutrient measurements at sea (Hydes et al., 2010).

2.3. Aerosol Sampling and Analysis

During the spring, aerosol samples were collected onto single 20 x 25 cm Whatman 41 filters (Fisher) using a high volume aerosol collector (Tisch TSP) operating at a flow rate of ~1 m^3 min^{-1} (Baker et al., 2007) and located on the deck above the bridge of RRS *Discovery*. Separation of particles into aerodynamic diameters greater than or less than 1 μm was achieved during the summer cruise using a Sierra-type cascade impactor, also using Whatman 41 (Fisher) slotted substrates and filters. Collection filters and slotted substrates were acid-washed before use with 0.5 M HCl (Aristar Grade, Fisher), followed by 0.1 M HCl (Aristar Grade, Fisher). Collection times for most samples were relatively long (2–3 days) because of low aerosol trace metal concentrations in the high-latitude North Atlantic, but samples collected under the Eyjafjallajökull ash plume (spring TM07-09; locations of aerosol sampling depicted in Figure S2 [SI]) were only collected for 1–3 hr. The collector was only used when the ship was heading into the prevailing wind in order to avoid contamination from the vessel.

Following collection, samples were sealed in plastic bags and immediately frozen at −20°C for return to the land-based laboratory. Trace elements were leached from the filters using a 1 M ammonium acetate solution (pH 4.7) and filtered through 0.2 μm filters (Minisart, Sartorius) (Baker et al., 2007) and their soluble concentrations were determined by ICP-OES and ICP-MS (Baker & Jickells, 2017). Total element concentrations were determined on portions of the filters by instrumental neutron activation analysis (INAA), with the two size fractions for the summer cruise samples combined together to give a single measurement (Sholkovitz et al., 2012) (Pb cannot be determined by INAA). Here we report on the dry deposition fluxes of soluble elements (F_{dry}, nmol m^{-2} day^{-1}) as the product of their aerosol concentrations (C_{aero}, pmol m^{-3}) and a dry deposition velocity (v_d) ($F_{dry} = C_{aero}\ v_d$). Values of v_d were set to 1 and 0.1 cm s^{-1} for the coarse (>1 μm) and fine (<1 μm) aerosol modes, respectively for summer cruise, and 0.7 cm s^{-1} for the spring cruise (Baker et al., 2007; Ganzeveld et al., 1998). Deposition velocities vary strongly as a function of particle size and wind speed (Ganzeveld et al., 1998) and are highly uncertain. An uncertainty in v_d of plus or minus a factor of 2–3 has been reported (Duce et al., 1991).

2.4. Diffusive Flux Measurements and Calculations

Turbulent kinetic energy dissipation (ε) was measured during summer cruise only using a free-fall microstructure shear profiler (MSS90L, Sea and Sun Technology GmbH). The rate of ε was calculated from the variance of the measured vertical microstructure shear by integration of the vertical microstructure shear power spectrum (Forryan et al., 2012) and assuming isotropic turbulence (Yamazaki & Osborn, 1990). Turbulent diffusivity (K) was estimated from ε and buoyancy frequency, full details of the approach are provided in (Painter et al., 2014). The top 8 m of data in the water column were omitted in order to remove near-surface influences prior to binning the diffusivity data into 4 m depth bins. Vertical diffusive fluxes of trace elements into surface mixed layer were subsequently determined from the turbulent diffusivity and profiles of the trace elements. The mixed layer depths (MLD) were obtained at the depth of the local maximum in the Brunt-Väisälä buoyancy frequency profile (MLD range 17–49 m, mean ± 1 standard deviation: 28 ± 8 m) (Painter et al., 2014).

2.5. Winter Convective Fluxes

Winter convective fluxes were obtained from examination of individual Argo float profiles from the IRB and IB in winter 2010, which allowed determination of the MLD using criteria by (de Boyer Montégut et al., 2004). The obtained mean winter MLD were 170 ± 100 m for the IRB and 355 ± 144 m for the IB, rounded to 200 and 350 m, respectively; full details are provided elsewhere (Painter et al., 2014). Dissolved metal concentrations from spring profiles in each basin were then integrated to the respective depth of winter mixing to obtain a mean estimate of convective inputs as reported previously (Nielsdottir et al., 2009). Limited spatial coverage of the IRB and IB by Argo floats introduced some uncertainty around the mean winter MLD which appeared spatially heterogenous whereas metal concentrations measured during the spring cruise at the mean winter MLD were more spatially homogenous. This latter observation suggests that convective fluxes obtained by blending mean winter MLD with spring metal concentrations is unlikely to be significantly in error due to the time gap between the two data sets.

3. Results and Discussion

3.1. Hydrography

The study region in the high-latitude North Atlantic Ocean includes the IB and IRB, Hatton-Rockall Plateau, and Rockall Trough and Reykjanes Ridge regions (Figure 1). The cyclonic subpolar gyre of the North Atlantic flows around the IRB and IB. The North Atlantic Drift (NAD) is part of the southern region of the subpolar gyre and flows as the main near-surface current northward into the central region of the high-latitude North Atlantic (between ~10°W and 30°W) with depths in the IB of up to 1 km (Bower et al., 2002). The NAD is bounded by the cooler Irminger Current to the west, with the southern and eastern boundaries weakly constrained by extensions of the North Atlantic Current (NAC) (Rossby et al., 1998). The NAD has a salinity range of 35.2–35.7 and is warmer than surrounding waters (Rossby et al., 1998). The Irminger Current is prominent in the east IRB, and turns west in the north IRB before moving south in the subpolar gyre flow. Trajectories of Argo floats released in our study region during RRS *Discovery* cruise D321 (June 2007) indicate the described upper ocean current movements (in SI, Figure S3). The western IRB features a fresh and cold western boundary current (East Greenland Current, EGC) with a southerly flow, and salinity and temperature ranges of 30–34°C and 3.5–5.5°C, respectively (Bacon et al., 2002).

Details of the water masses in our research area are discussed in the SI and shown in Table S2 (SI), and were used to support the interpretation of the potential temperature-salinity (θ-S) plot (SI, Figure S4), optimum multiparameter (OMP), water mass analysis (Tomczak, 1999) for an east-west section along 60°N (SI, Figure S5), and trace metal distributions.

3.2. Surface Water Distributions of Dissolved and Total Dissolvable Trace Elements

A total of 195 surface samples were collected using the tow fish in the IB and IRB during the cruises. For off shore stations (water depth >400 m) the ranges and average surface water concentrations of nitrate + nitrite (TON), dissolved and total dissolvable trace elements for the spring and summer cruises are presented in Table 1, for the whole region and separately for the IB and IRB.

In surface waters, a gradient of decreasing TON and phosphate concentrations from northwest to southeast was observed for the spring cruises (Figure 2). This trend was also observed for DAl, DCd, DCo, DCu, DNi, DPb, DMn, and DZn and was likely due to their active and/or passive biological uptake in relation to the general spatial progression of the spring bloom from east to west in the subpolar North Atlantic (Olsen et al., 2008), which was consistent with in situ and satellited derived chlorophyll data for 2013 (Ryan-Keogh et al., 2013). In addition, ash-derived metal inputs from the Eyjafjallajökull volcanic eruption phase during spring could have contributed to an increase in concentrations for a range of elements associated with the ash particles (Achterberg et al., 2013). There were elevated concentrations for a range of elements (DAl: 45 nM; DMn: 3.20 nM, TDMn 8.78 nM; DZn: 0.625 nM, TDZn 1.30 nM) directly under the volcanic plume (63.1°N, 18.5°W) in the immediate vicinity of the Icelandic coast (Table 1), but with no increases for Co, Cd, Cu, Ni, and Pb compared with surface waters that were not influenced by the volcanic ash inputs (further discussion is provided in aerosol section below). Enhanced DAl, DCd, DCo, DCu, DPb, DNi, DMn, and DZn concentrations were also observed on the Scottish Shelf (Figure 2), likely due to continental and benthic inputs; indeed the elevated DMn (8.73 nM) on this shelf provided a strong indication of benthic release (Birchill et al., 2019; Burdige, 1993).

Spatial variability in open ocean areas during spring was observed for surface water concentrations of trace metals (Figure 2), which may be related to the temporal and spatial variability in ash deposition (Achterberg et al., 2013) and possibly (sub-)mesoscale processes, including fronts and eddies (Lévy et al., 2012). The total dissolvable metals showed similar patterns to dissolved metals, with generally lower concentrations in the southeast of the area where the bloom was already well progressed (Ryan-Keogh et al., 2013), but a less pronounced concentration increase toward the northwest (Figure 2). The strongest relationships between dissolved and labile particulate elements (total dissolvable minus dissolved) were observed for Cd (−0.51), Cu (−0.57), and Ni (−0.54) (bivariate Pearson Correlation) indicating a transfer of the dissolved forms of these elements to particulate forms.

During the summer cruise (Figure 3), phosphate and TON still showed a west to east decrease in concentrations, with anomalously high TON depletion in the IB, potentially as a result of the relief in Fe limitation of

Table 1
Ranges and Average Concentration Values for TON and Dissolved and Total Dissolvable Trace Elements in Surface Waters of the High-Latitude North Atlantic (Excluding Shelf Waters)

	Range	Average all (±SD)	Average IB (±SD)	Average IRB (±SD)	*t* test (IRB vs. IB)	*t* test *P* value (seasonal comparison IB)	*t* test *P* value (seasonal comparison IRB)
Spring cruises							
DCo (pM)	22.9–109	52.8 (±11.0) $n = 103$	52.2 (±7.49) $n = 45$	50.7 (±5.65) $n = 20$	0.40	0.00	0.00
TDCo (pM)	72.2–336	97.4 (±36.1) $n = 64$	98.4 (±46.5) $n = 29$	95.6 (±5.29) $n = 7$	0.75	0.009	0.03
DMn (nM)	0.22–8.73	0.72 (±1.06) $n = 103$	0.52 (±0.09) $n = 45$	0.48 (±0.07) $n = 20$	0.025	0.015	0.006
TDMn (nM)	0.48–10.5	1.42 (±2.14) $n = 64$	1.12 (±1.83) $n = 29$	0.77 (±0.39) $n = 7$	0.098	0.31	0.25
DCd (pM)	36.9–197	125 (±41.7) $n = 103$	118 (±32.0) $n = 45$	170 (±17.4) $n = 20$	0.00	0.00	0.00
TDCd (pM)	102–313	181 (±42.0) $n = 69$	195 (±47.6) $n = 29$	170 (±29.7) $n = 7$	0.098	0.00	0.19
DCu (nM)	0.70–2.28	1.16 (±0.19) $n = 103$	1.14 (±0.11) $n = 45$	1.16 (±0.03) $n = 20$	0.26	0.00	0.00
TDCu (nM)	0.96–2.16	1.21 (±0.23) $n = 69$	1.17 (±0.15) $n = 29$	1.21 (±0.06) $n = 7$	0.30	0.015	0.002
DNi (nM)	1.41–4.14	3.23 (±0.31) $n = 103$	3.32 (±0.22) $n = 45$	3.18 (±0.24) $n = 20$	0.038	0.00	0.00
TDNi (nM)	2.75–7.05	3.80 (±0.48) $n = 69$	3.76 (±0.16) $n = 29$	3.91 (±0.09) $n = 7$	0.0046	0.04	0.85
DZn (nM)	0.07–1.24	0.32 (±0.16) $n = 97$	0.29 (±0.14) $n = 41$	0.33 (±0.11) $n = 20$	0.23	0.00	0.00
TDZn (nM)	0.09–7.19	0.74 (±0.89) $n = 64$	0.64 (±0.36) $n = 28$	1.62 (±2.46) $n = 7$	0.33	0.00	0.23
DAl (nM)	0.27–44.8	3.44 (±5.64) $n = 105$	2.51 (±1.87) $n = 45$	2.60 (±2.08) $n = 20$	0.88	0.00	0.00
DPb (pM)	14.8–36.3	23.4 (±3.87) $n = 103$	21.9 (±3.33) $n = 45$	25.0 (±2.02) $n = 20$	0.00	0.00	0.00
TDPb (pM)	20.9–99.3	30.7 (±14.2) $n = 69$	29.3 (±15.6) $n = 29$	27.7 (±1.97) $n = 7$	0.59	0.006	0.03
NO_3 (μM)	4.94–14.5	9.96 (±2.54) $n = 94$	9.08 (±1.82) $n = 43$	12.6 (±0.99) $n = 19$	0.00	0.00	0.00
Summer cruise							
DCo (pM)	20.6–46.1	37.6 (±11.0) $n = 84$	32.3 (±5.69) $n = 25$	40.8 (±11.1) $n = 42$	0.00		
TDCo (pM)	5.3–117	75.3 (±23.3) $n = 35$	71.4 (±9.7) $n = 5$	76.6 (±30.0) $n = 15$	0.57		
DMn (nM)	0.24–1.35	0.43 (±0.15) $n = 84$	0.46 (±0.09) $n = 25$	0.41 (±0.11) $n = 20$	0.029		
TDMn (nM)	0.03–1.96	0.72 (±0.31) $n = 35$	0.76 (±0.16) $n = 5$	0.69 (±0.28) $n = 15$	0.49		
DCd (pM)	4.45–93.7	30.2 (±19.9) $n = 87$	18.5 (±11.2) $n = 26$	37.6 (±17.1) $n = 44$	0.00		
TDCd (pM)	55.9–274	144 (±62.3) $n = 41$	107 (±31.6) $n = 10$	191 (±40.5) $n = 15$	0.00		
DCu (nM)	0.85–1.83	0.97 (±0.14) $n = 87$	0.93 (±0.04) $n = 26$	0.99 (±0.13) $n = 44$	0.006		
TDCu (nM)	0.97–1.65	1.10 (±0.11) $n = 41$	1.08 (±0.07) $n = 10$	1.09 (±0.04) $n = 15$	0.62		
DNi (nM)	2.09–3.44	2.75 (±0.23) $n = 85$	2.65 (±0.25) $n = 26$	2.83 (±0.18) $n = 42$	0.003		
TDNi (nM)	3.11–4.33	3.72 (±0.32) $n = 41$	3.53 (±0.29) $n = 10$	3.89 (±0.25) $n = 15$	0.004		
DZn (nM)	0.02–0.23	0.065 (±0.05) $n = 68$	0.060 (±0.06) $n = 19$	0.069 (±0.056) $n = 37$	0.59		

Table 1
Continued

	Range	Average all (±SD)	Average IB (±SD)	Average IRB (±SD)	*t* test (IRB vs. IB)	*t* test *P* value (seasonal comparison IB)	*t* test *P* value (seasonal comparison IRB)
TDZn (nM)	0.02–4.65	0.40 (±0.81) $n = 34$	0.15 (±0.13) $n = 5$	1.09 (±0.04) $n = 15$	0.15		
DAl (nM)	0.10–4.81	0.94 (±0.84) $n = 89$	1.22 (±0.72) $n = 26$	0.056 (±0.73) $n = 43$	0.00		
DPb (pM)	10.1–104	17.7 (±9.64) $n = 87$	16.0 (±2.86) $n = 26$	16.4 (±1.57) $n = 44$	0.55		
TDPb (pM)	16.8–37.9	23.7 (±4.3) $n = 41$	20.6 (±1.9) $n = 10$	24.6 (±4.3) $n = 15$	0.004		
NO_3 (μM)	BD– 6.47	2.24 (±1.66) $n = 74$	0.57 (±0.76) $n = 21$	2.86 (±1.47) $n = 40$	0.00		

Note. A regional concentration comparison between the Iceland (IB) and Irminger (IRB) Basins is presented, as well as a seasonal comparison between the spring (D350/351) and summer cruise (D354) of 2010 for each basin; Student *t* test was undertaken with a 95% significance threshold. BD: below detection limit.

primary productivity by the additional Fe supply from volcanic ash inputs (Achterberg et al., 2013). Open ocean concentrations in the study region of DAl, DCd, DCo, DCu, DMn, DPb, and DZn were lower than in spring (Figures 2 and 3 and Table 1). The coastal stations off Scotland and Iceland (Figure 3) did not show elevated dissolved metal concentrations as observed during the spring cruises, with the reduction in concentrations likely the consequence of biological and physico-chemical removal (precipitation and scavenging for Al, Pb, and Mn), and lower atmospheric inputs in the Icelandic waters following the termination of the Eyjafjallajökull eruption (22 May 2010; Gudmundsson et al., 2012). Total dissolvable metal concentrations in the overall study region also showed reductions in average summer concentrations relative to spring (Figures 2 and 3 and Table 1), likely related to export of particles from the surface ocean. For the summer cruise strongest relationships between dissolved and labile particulate elements were observed for Cu (−0.70) with the rest of the elements showing $r < 0.29$.

Contributions of average dissolved to total dissolvable elemental concentration ratios for spring (first number) and summer (second number) were Co (54% and 50%), Mn (50.5% and 60%), Ni (85% and 74%), Cd (69% and 21%), Pb (76% and 75%), Zn (43% and 16%), and Cu (96% and 89%). This indicates that in the surface ocean Ni, Pb, and Cu (Cd spring only) were largely present in the dissolved forms, but around half or more of Co, Mn, Zn, and Cd (Cd summer only) were in the particulate form, and likely incorporated in biogenic material (Cd and Zn; Bruland et al., 2014), or onto biogenic material through bacterial mediated precipitation (Mn and Co; Moffett & Ho, 1996; Tebo et al., 2004).

We compared average surface water dissolved and total dissolvable metal concentrations between the IB and IRB, as well as between spring and summer for the individual basins (Table 1). We included TON to determine the effects of biological uptake. The *t* tests indicated significant differences in spring between the IB and IRB for DCd and DPb, and in summer for DCo, DCd, DCu, and DNi, with lower concentrations in the IB compared with the IRB. Nitrate was also significantly lower in the IB compared to the IRB (by 1.34-fold in spring and fivefold in summer), with the depleted levels in the IB explained by enhanced TON removal as a result of the ash-derived Fe inputs (Achterberg et al., 2013) resulting in Fe and TON co-limited microbial communities (Ryan-Keogh et al., 2013).

For both the IRB and IB, all of the dissolved metals measured showed significant reductions in average summer concentrations relative to spring (Table 1). Furthermore, the *t* tests indicated significant differences in spring between the IB and IRB for TDNi, and in summer for TDCd, TDNi, and TDPb, with lower concentrations in the IB compared with the IRB (Table 1). Total dissolvable metal concentrations showed significant reductions for the individual basins in average summer concentrations relative to spring for Cd, Ni, Zn (IB only), Co, Cu, and Pb (IB and IRB), but not for Mn (Table 1).

There is a paucity of surface ocean data for elements other than Fe and Al for our study region; comparison between our summer DAl data set (0.94 ± 0.837 nM; not influenced by volcanic ash inputs; Table 1) and that from a CLIVAR cruise (A16N in 2003, Al < 2 nM) indicates a reasonable agreement (Measures et al., 2008).

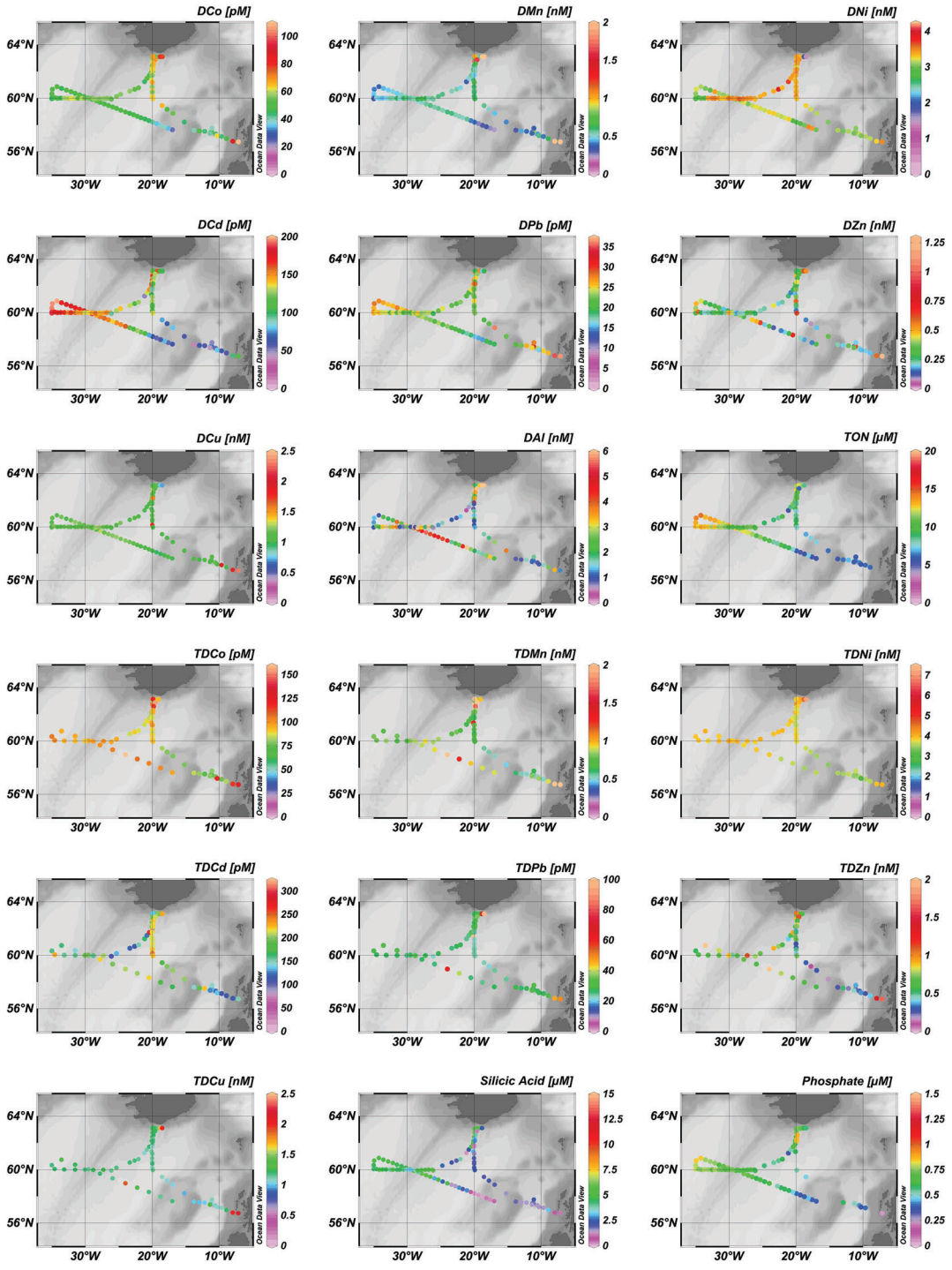

Figure 2. Surface water concentrations (as labeled) of dissolved and total dissolvable Co, Mn, Ni, Cd, Pb, Zn, Cu, and Al and nitrate + nitrite (TON), silicic acid, and phosphate during spring 2010 (D350 and D351). Figures were produced using Ocean Data View (Schlitzer, R., Ocean Data View, odv.awi.de, 2017).

Mean values of the significant differences between spring and summer dissolved concentrations for multiple elements (Table 1), including Fe (Achterberg et al., 2018), could be used to calculate a net removal ratio (Table 2; in mmol metal:mol P). This apparent net export stoichiometry was very similar between the two basins for the majority of elements and, for the bio-essential metals (Fe, Ni, Zn, Cu, Fe, Cd, Mn, and Co),

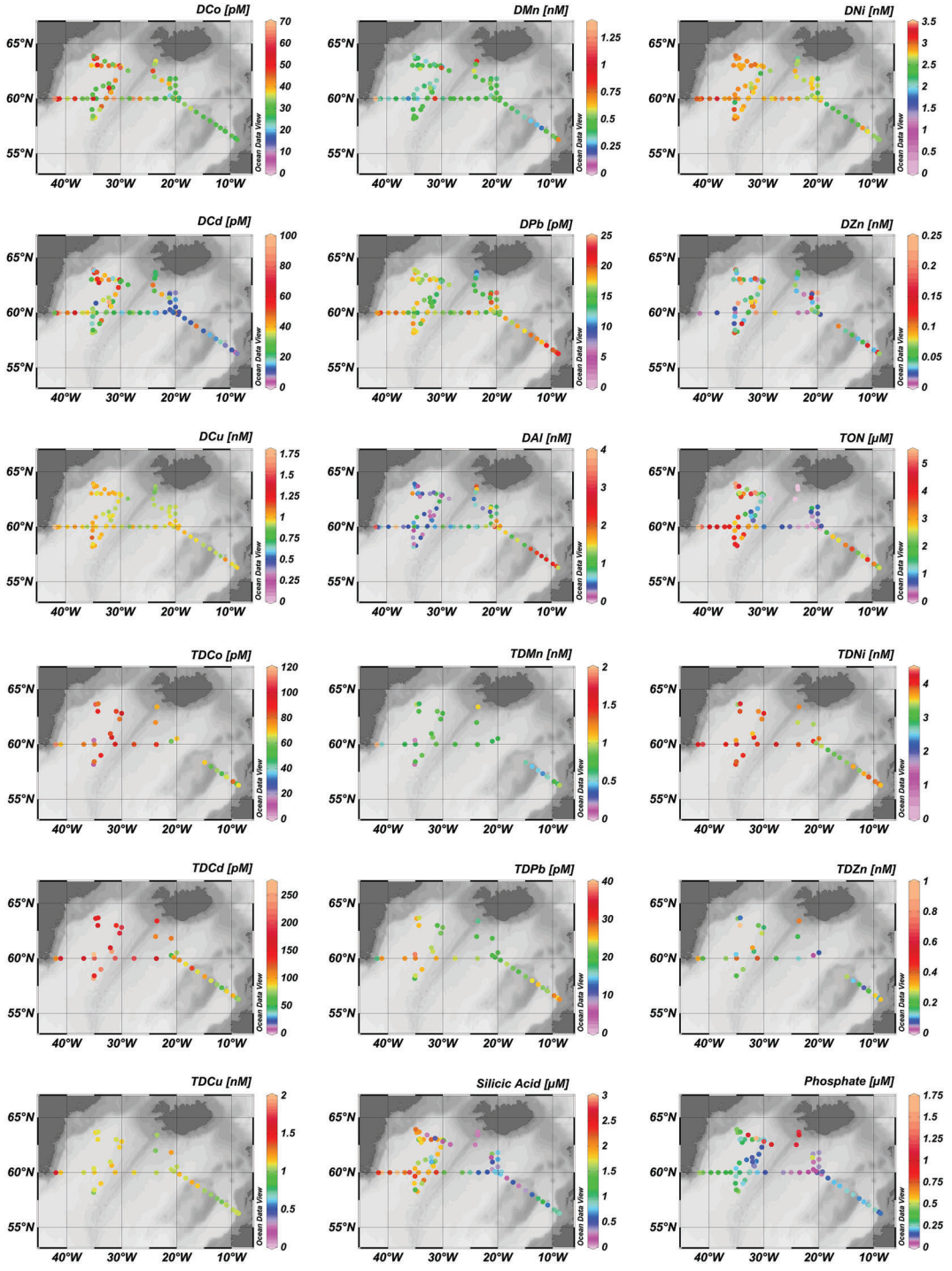

Figure 3. Surface water concentrations (as labeled) of dissolved and total dissolvable Co, Mn, Ni, Cd, Pb, Zn, Cu, and Al and nitrate + nitrite (TON), silicic acid, and phosphate during summer 2010 (D354). Figures were produced using Ocean Data View (Schlitzer, R., Ocean Data View, odv.awi.de, 2017).

was broadly consistent with what might be expected on the basis of biological dominance of removal (Twining & Baines, 2013). Interestingly, apparent Fe removal stoichiometry was higher in the IB than the IRB, potentially due to the more Fe limited status of the latter (Ryan-Keogh et al., 2013) and higher Fe inputs to the former (Achterberg et al., 2013).

Table 2
Removal and Supply Ratios (in mmol:mol P) of Dissolved Trace Elements Relative to P (phosphate) Out of and Into the Surface Waters of the Iceland Basin (IB) and Irminger Basin (IRB)

	Removal ratio IB	Removal ratio IRB	Supply ratio IB	Supply ratio IRB
DAl	2.43	4.16	8.24	5.93
DNi	1.26	0.57	4.49	5.03
DZn	0.43	0.43	1.01	1.10
DCu	0.39	0.28	1.24	1.54
DFe	0.27	0.06	0.94	0.25
DCd	0.19	0.22	0.25	0.28
DMn	0.10	0.11	0.81	0.79
DCo	0.037	0.016	0.10	0.11
DPb	0.011	0.014	0.04	0.04

Note. Removal ratios were calculated from the differences between spring and summer 2010 surface water concentrations (Table 1), and supply ratios were determined from winter convective mixing (Table 5), which was the dominant supply mechanism for dissolved elements. Dissolved Fe data were obtained from Achterberg et al. (2018) and P supply data (convective mixing) from Painter et al. (2014).

3.3. Concentration Profiles of Dissolved and Total Dissolvable Elements

Depth profiles of dissolved and total dissolvable elements for a station in the IRB are presented in order to illustrate the similarities and contrasts in their behaviors in the water column in the high-latitude North Atlantic (Figure 4).

The overall trend in dissolved Al, Cd, Co, Cu, Ni, and Zn shows depleted surface ocean concentrations with an increase with depth. This behavior is similar to that of the macronutrients (TON, phosphate and silicic acid; Figure 4) and indicates involvement of biological processes in cycling of these elements, with surface water uptake (passive or active) by microbial organisms and deep water remineralization following vertical transfer of biogenic material to depth (Bruland et al., 2014; Menzel Barraqueta et al., 2018) and/or transport of nutrient-rich deep waters that have collected particles upstream (Middag et al., 2018, 2019); further discussion provided in section on convective supply. The depth distribution of Cd shows strong similarities to those of TON and phosphate, in agreement with other observations (Middag et al., 2018). The distributions of DZn, and to a large extent DAl, showed similarities to silicic acid (Menzel Barraqueta et al., 2018; Middag et al., 2019), potentially suggesting an involvement in processes related to opal production and dissolution (e.g., by diatoms). The surface removal at station 17 for DCo, DCu, and DNi (Figure 4) was not as pronounced as for DCd and DZn, which is in agreement with other reports and indicated a less pronounced uptake by phytoplankton relative to available stocks in conjunction with a sufficient supply and/or the presence of a fraction of the element which is difficult to assimilate due to ligand binding or slow kinetic dissociation processes (Bruland & Franks, 1983; Martin et al., 1993; Middag et al., 2020). Some combination of these processes is also likely to be responsible for observed residual DCo, DCu, and DNi concentrations at depleted nutrient concentrations (non-zero intercepts in element-nutrient plots Figures S6–S8). Iron is presented here to allow comparison to other elements, and shows DFe surface depletion and relatively constant DFe concentrations (0.7–0.9 nM) at depth, with increasing TDFe levels (Achterberg et al., 2018). DMn and DPb also have low surface water concentrations and feature increases in concentrations in the first tens to hundreds of meters of the water column. These trends are likely associated with photoreduction (Mn only; Sunda et al., 1983) and remineralization of sinking material with release of the elements, and the presence of waters perturbed by atmospheric anthropogenic Pb inputs and ventilated over the last decades (mode waters in IRB [0–1,000 m], Labrador Seawater [500–2,500 m]; Boyle et al., 1986; Zurbrick et al., 2018). A decrease in DMn and DPb concentrations is evident at greater depths and linked to DMn removal through MnO_x formation (Wu et al., 2014), and scavenging of DPb onto particles in addition to presence of water masses less perturbed by historical anthropogenic Pb inputs (Boyle et al., 1986; Echegoyen et al., 2014). High DAl concentrations near the seafloor most likely represents the influence of the nepheloid layer of resuspended sediments, which is also reflected by the very high TDAl and TDFe concentrations (up to 27.2 nM Al and 8.39 nM Fe; Figure 4) in that part of the water column.

The difference between dissolved and total dissolvable concentrations was relatively small for the so-called "nutrient-type" elements (Cd, Co, Cu, Ni, and Zn) and also Pb, and more pronounced for Al, Mn, and Fe (Figure 4). This is reflected in the contributions of average dissolved to total dissolvable elemental concentration ratios for the full IBIS data set: Al (23%), Mn (66%), Co (74%), Ni (89%), Cd (85%), Pb (88%), Zn (85%), and Cu (96%). These findings indicate that in the water column the bio-essential elements (Cd, Cu, Ni, and Zn) that are directly involved in microbial functioning, occur largely in the dissolved phase in waters below the euphotic zone as a consequence of rapid remineralization of sinking biogenic matter with only a minor fraction forming part of biogenic particles. Whereas elements that form an important part of lithogenic (Al), skeletal (Al; Gehlen et al., 2002), metal oxide (Mn and Co; Moffett & Ho, 1996) material had a larger labile particulate fraction as also reported for Fe (14%; Achterberg et al., 2013). The oceanic Pb concentrations are dominated by anthropogenic aerosol inputs (Bridgestock et al., 2016; Wu & Boyle, 1997), with an apparent high solubility of the land-derived combustion related atmospheric aerosols (Chester et al., 1993), and a large fraction of Pb in the dissolved phase in our study region.

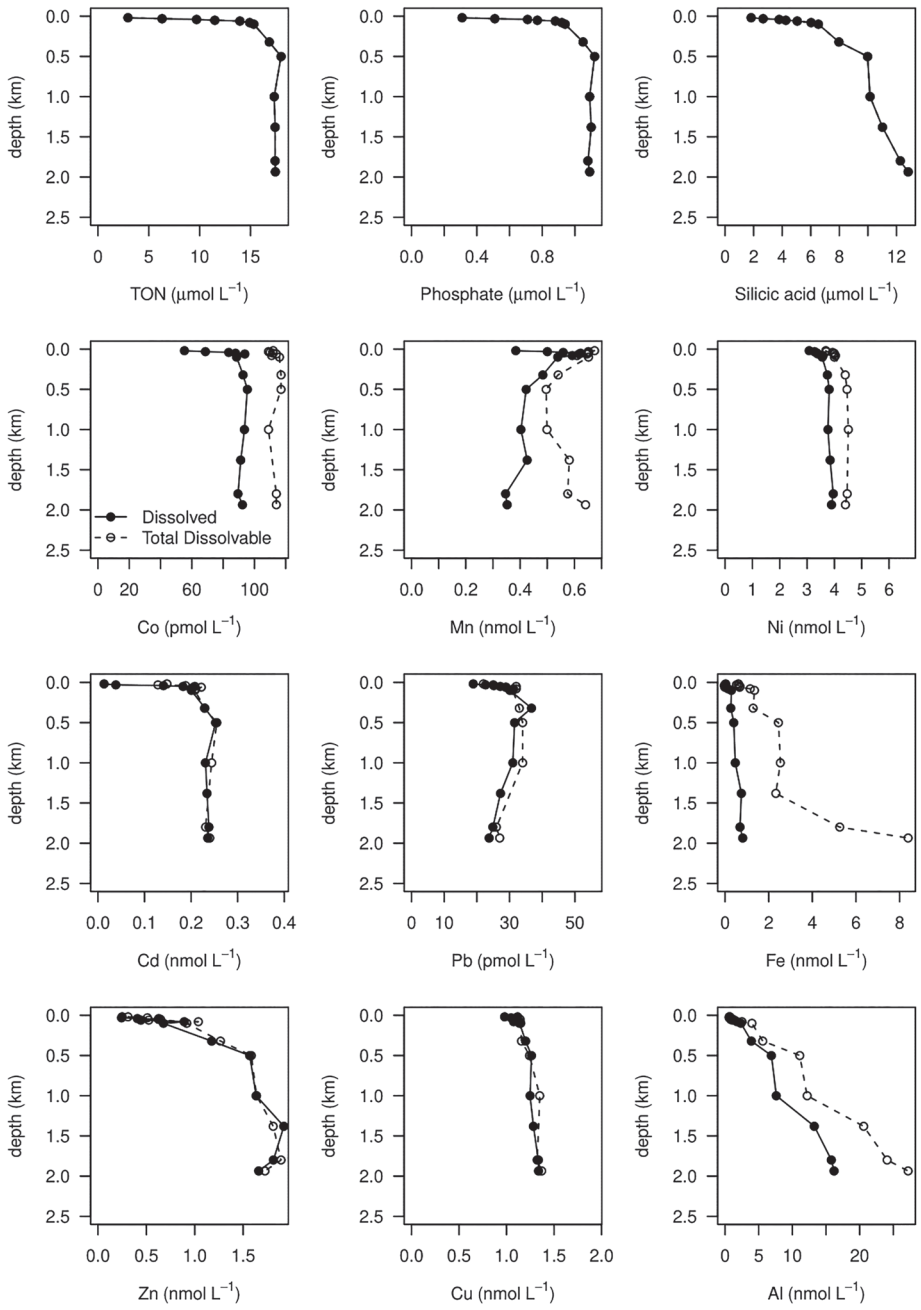

Figure 4. Depth profiles for nitrate + nitrite (TON), phosphate, silicic acid, and dissolved (filled circles) and total dissolvable (open circles) Co, Mn, Ni, Cd, Pb, Fe, Zn, Cu, and Al (as labeled) for station 17 (63.01°N, 34.97°W) sampled in IRB during summer 2010 (D354).

A recent GEOTRACES section in the South Pacific (GP16; Schlitzer et al., 2018) allows a comprehensive comparison to our study and reports dissolved to total (dissolved + particulate) elemental concentration ratios for open ocean regions remote from land: Zn (~50–98%), Pb (~80–95%), Mn (~66–90%), Cu (90–95%), Co (~80–98%), Cd (~95–99%), and Ni (92–99%). Our dissolved:total ratio observations are in good agreement with these South Pacific findings. Particulate elemental concentrations (Co: up to ~2–3 pM; Mn: up to ~90 pM; Cd: up to ~2–3 pM; Al: up to ~4 nM) for a mid-latitude North Atlantic GEOTRACES transect (GA03) (Twining et al., 2015) were also in good agreement with our labile particulate values.

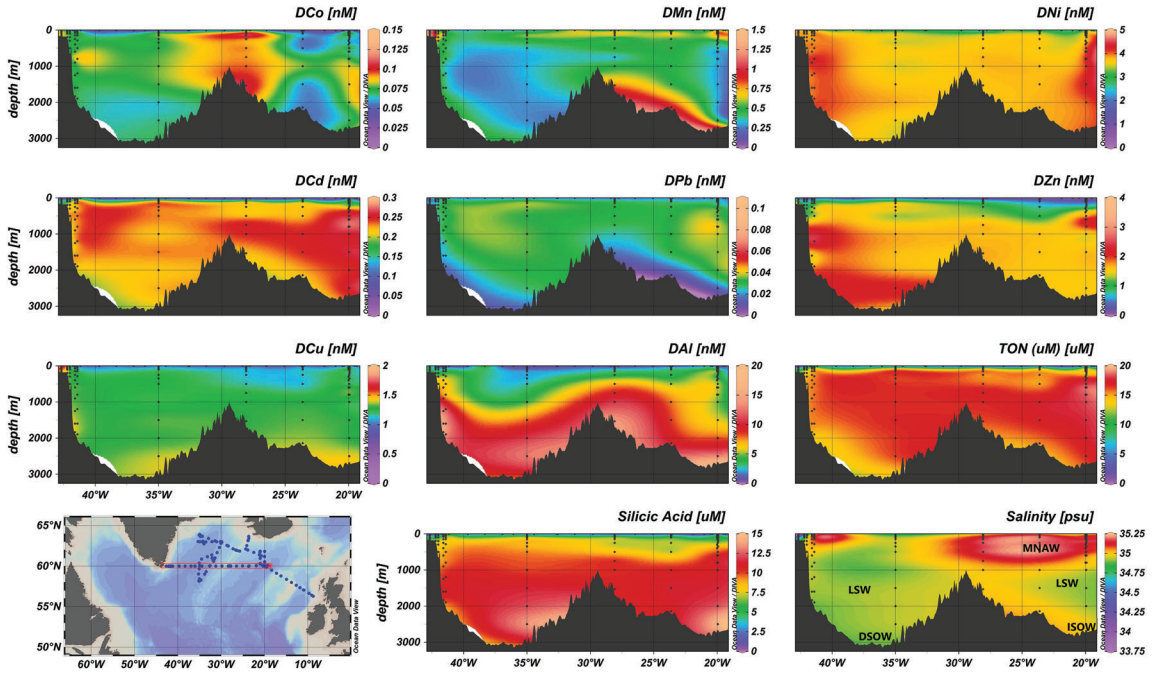

Figure 5. Section plots of dissolved trace elements, nitrate + nitrite (TON), silicic acid, and salinity on a transect along 60°N with data from summer 2010. Main water masses indicated in salinity panel and explained in SI Text S2. MNAW: Modified North Atlantic Water; LSW: Labrador Seawater; ISOW: Iceland-Scotland Overflow Water; DSOW: Denmark Strait Overflow Water. Figures were produced using Ocean Data View (Schlitzer, R., Ocean Data View, odv.awi.de, 2017).

3.4. Ocean Sections of Dissolved and Total Dissolvable Trace Elements

Four transects were sampled at a high spatial resolution in 2010, the first during the spring cruise (D350) and the others during the summer cruise (D354). Sections for dissolved elements for the D354 transects are presented here, and the dissolved elements for D350 and total dissolvable elements for all transects are presented in the SI. The first and second transect were along ~60°N, between 20 and 35°W (D350) and 19 and 43°W (D354), respectively, crossing the Reykjanes Ridge at ~29°W (Figure 5, and SI, Figure S9). The third transect was from 20 to 35°W and 60°N to 63°N and crossed the Reykjanes Ridge at about 62°N (Figure 6). The fourth section was along 60°N from 41.4°W onto the Greenland shelf (Figure 7).

Figure 5 and Figure S9 (SI) allow for a comparison between subsurface concentrations (down to ~600–800 m) in the IB between spring and summer cruises, during and after the volcanic eruption. In the case of TDFe (Achterberg et al., 2018), higher concentrations were observed in the IB in the top ~600 m in spring during the eruption compared to the summer cruise. For the elements which showed a surface water enhancement due to the ash inputs (Al, Mn, and Zn; see Figure 2, and SI Figures S9 and S10), there was no clear evidence of increases in dissolved or total dissolvable concentrations in subsurface waters.

Deep ocean water masses in the study area are all relatively young (i.e., recently ventilated) and have not yet accumulated much remineralized elements and therefore elemental signatures of the water masses are not as pronounced as further south in the Atlantic (e.g., Middag et al., 2018). The nutrient-type elements (Cd, Cu, Ni, and Zn) showed increases in dissolved concentrations with depth, also reflected by total dissolvable distributions (see SI Figures S10–S12). Concentrations of DZn were lowest in Modified North Atlantic Water (MNAW [see SI]; 0.3–0.8 nM) and increased gradually (to ~1.8–2.0 nM) in deeper Labrador Seawater (LSW), Iceland-Scotland Overflow Water (ISOW), and Denmark Strait Overflow Water (DSOW) (Figures 5 and 6, and SI Text S2 for water masses), in agreement with reports from the GEOTRACES GA02 section (Middag et al., 2019). A shallower increase in DCd was observed, relative to Zn, as also indicated in Figure 4, with concentrations in the deeper waters reaching ~0.24 nM; these observations agree with those (0.2–0.26 nM for North Atlantic Deep Water [NADW] in IRB north of 60°N) reported for the GEOTRACES GA02 section (Middag et al., 2018). Dissolved Cu showed a concentration increase with depth that was intermediate between Zn and Cd, likely related to its hybrid behavior associated to scavenging upon release following remineralization (Bruland et al., 2014). Similar DCu trends in the water column are also

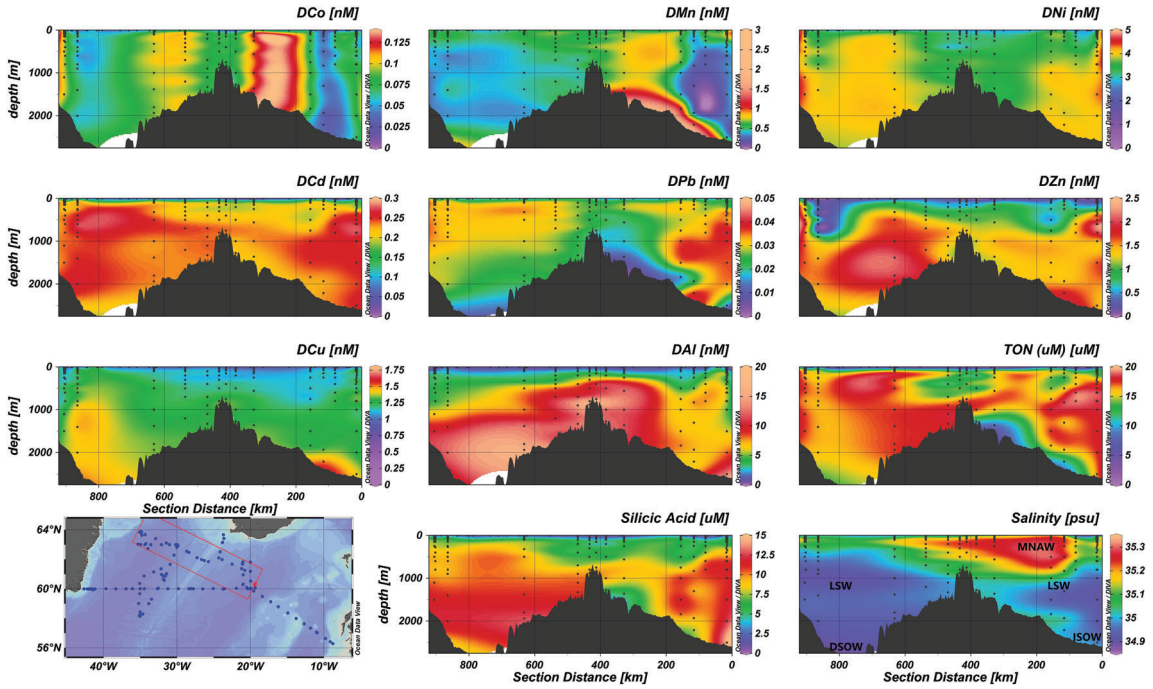

Figure 6. Section plots of dissolved trace elements, nitrate + nitrite (TON), silicic acid, and salinity on a transect across the Reykjanes Ridge at 62°N with data from summer 2010. Main water masses indicated in salinity panel and explained in SI Text S2. MNAW: Modified North Atlantic Water; LSW: Labrador Seawater; ISOW: Iceland-Scotland Overflow Water; DSOW: Denmark Strait Overflow Water. Figures were produced using Ocean Data View (Schlitzer, R., Ocean Data View, odv.awi.de, 2017).

shown in Cu isotope studies indicating preferential removal of lighter isotopes onto particles (Little et al., 2018; Takano et al., 2014). Nevertheless, the difference between TDCu and DCu was small in deep waters (Figure 4) indicating a small particulate Cu stock. Deep water DCu concentrations ranged between 1.40–1.60 nM and agree with those reported for the NW Atlantic of 1.70 nmol kg^{-1} (Bruland & Franks, 1983). Maxima in DCu of ~1.70 nM in bottom waters (e.g., Figure 5), also reflected in TDCu maxima of up to ~1.9 nM, were associated with DSOW and ISOW with likely additional benthic inputs of Cu as suggested by (Boyle et al., 1977), and also indicated in a Cu isotope study (Little et al., 2018). Similar to DCu, the surface water concentrations of DNi were not strongly depleted with concentrations always >1.4 nM. DNi showed a shallower remineralization compared to DCu, and lower concentrations in the MNAW than the LSW or DSOW/ISOW. The DNi concentration in our study agree well with values ranging between 3.6 and 4.2 nM in DSOW and LSW reported by (Middag et al., 2020). As indicated in Figure 4, the difference between TDNi and DNi was noticeable and showed that Ni has a larger particulate stock compared with Cd, Cu or Zn. Between ~5% and 20% of TDNi occurred in a reactive particulate form in the water column, with highest fractions in the top of the water column, likely associated with biogenic material. Nevertheless, the remnants of a particulate Ni fraction at depth, indicates that not all Ni is associated with a biogenic fraction that can be readily remineralized by microbial processes. The particulate fraction is unlikely to be lithogenic, as much higher particulate Fe values would be expected throughout the water column than reported for this study (Achterberg et al., 2018). Assuming congruent dissolution of Fe and Ni from crustal origin (Wedepohl, 1991) or ash from the Eyjafjallajökull volcano (Achterberg et al., 2013), this would supply between 1,300 and 1,600 times more Fe relative to Ni, and there is no evidence of this (see Figure 5). Particulate Ni therefore appears to be locked up in an unknown organic fraction.

The DAl concentrations ranged between ~2 nM in surface waters to 24 nM at depth, with some spatial variability and highest concentrations in the ISOW and DSOW (e.g., Figure 5) and are in good agreement with those reported (~1.7–23 nM) for the IB and IRB (Menzel Barraqueta et al., 2018). Increases of DAl with depth have been related to sinking opaline material and dissolution at depth as reflected in Si distributions (Gehlen et al., 2002; Menzel Barraqueta et al., 2018), and agree with observations in the Mediterranean

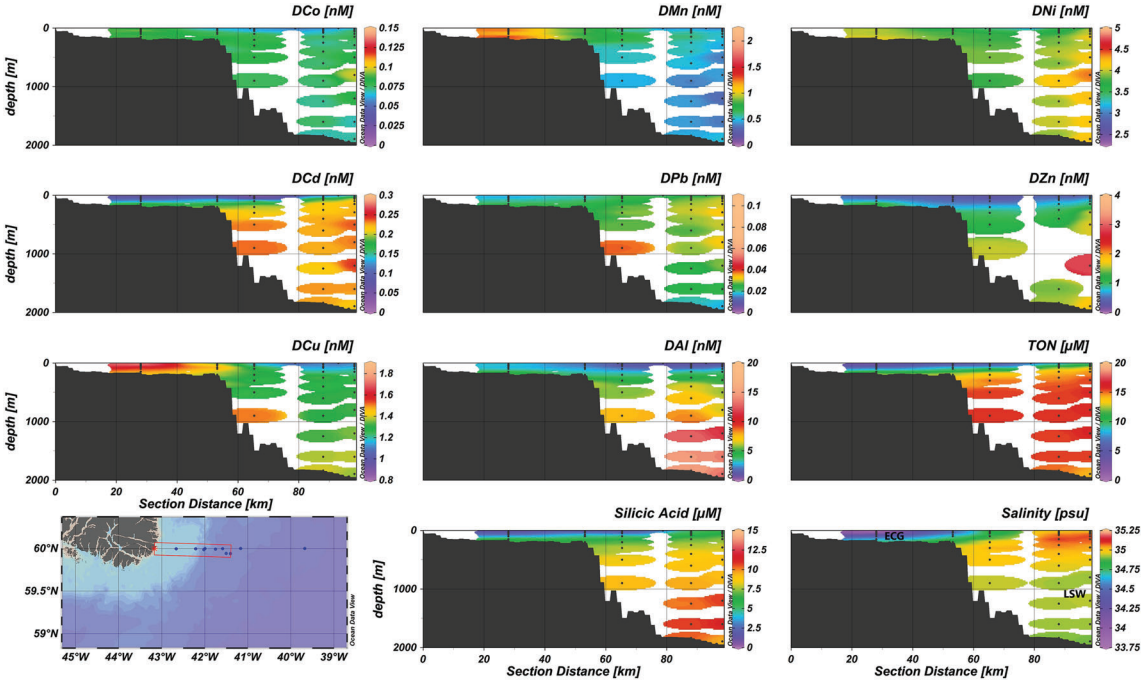

Figure 7. Section plots of dissolved trace elements, nitrate + nitrite (TON), silicic acid, and salinity on a transect along 60°N onto the Greenland shelf with data from summer 2010. Main water masses indicated in salinity panel and explained in SI Text S2. ECG: East Greenland Current; LSW: Labrador Seawater. Figures were produced using Ocean Data View (Schlitzer, R., Ocean Data View, odv.awi.de, 2017).

(Rolison et al., 2015). Our observations contrast with distributions displaying elevated DAl in surface waters, associated with atmospheric inputs, and decreases with depth related to scavenging, as has been observed in the low-latitude North Atlantic (Measures et al., 2015) and Pacific Ocean (Orians & Bruland, 1986).

Enhanced DPb was observed in LSW with concentrations up to ~30–40 pM (e.g., Figures 5 and 7). Similar observations of elevated DPb in LSW have previously been reported (Zurbrick et al., 2018) and attributed to historical atmospheric anthropogenic Pb inputs to the N Atlantic. Lower DPb concentrations in ISOW and DSOW (5–15 pM; Figures 5 and 6) agree with those reported by (Zurbrick et al., 2018). The dynamic behaviors of Co and Mn, with strong input and removal processes, coupled to the presence of relatively young water masses in the high-latitude North Atlantic, meant that no distinct elemental signatures could be observed in the various water masses (Figures 5 and 6).

An important feature along the three deep ocean sections is the elevated concentrations of DMn (up to 0.96 nM), TDMn (up to 3.25 nM), DCo (up to 94 pM), TDCo (up to 135 pM), DAl (up to 19 nM), and TDAl (up to 104 nM) over the Reykjanes Ridge (also associated with enhanced DFe [up to 1.03 nM] and TDFe [up to 57 nM]; Achterberg et al., 2018), particularly on the eastern flank. The elevated concentrations are likely largely driven by enhanced turbulent mixing over the Reykjanes Ridge with resuspension of sunken particles, with perhaps a contribution by hydrothermal inputs (Achterberg et al., 2018). Internal tides, near-inertial waves and mean flows cause the deep turbulent mixing over the rough topography of mid-ocean ridges (Clément et al., 2017; St Laurent & Thurnherr, 2007). The mixing over the Reykjanes Ridge will transfer sedimented particulate material into the water column, with associated dynamic exchange of dissolved Mn, Co, and Al (and Fe). Removal of DPb through particle scavenging is evident in the vicinity of the Reykjanes Ridge, with concentrations down to 16.5 pM. Similar observations of depleted DPb (~7 pM) have been reported over the Mid-Atlantic Ridge (at TAG) for GEOTRACES cruise GA03 (Noble et al., 2015).

The fourth section was from 41.4°W along 60°N onto the Greenland shelf (Figure 7). The redox sensitive element Mn showed elevated surface dissolved concentrations of 0.35 nM at ~60 km off the coast and increasing to >1.35 nM at ~30 km off the coast (also see Figure 3). The DMn increase in coastal waters

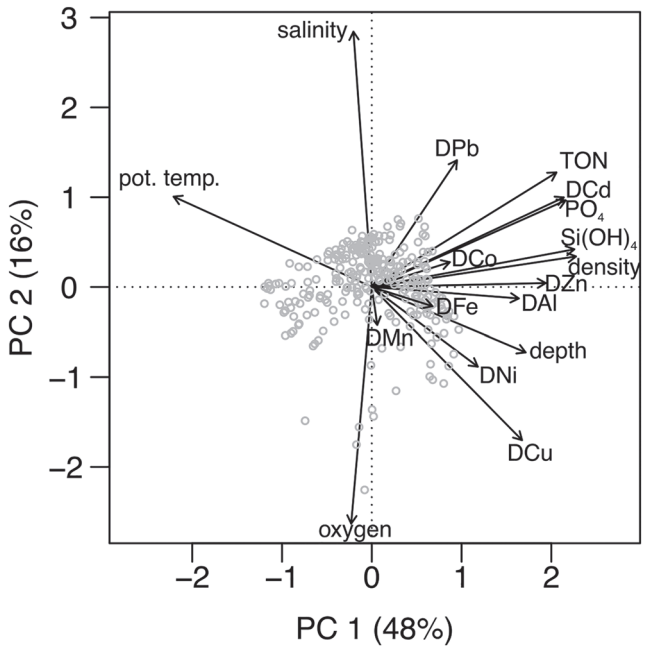

Figure 8. Principal component analysis for IBIS data set. Component scores of each sample are shown as gray circles. Principal component loadings for each variable are shown by black vectors. Loadings/scores have been scaled symmetrically by the square root of eigenvalues.

was coincident with a reduction in salinity indicating the occurrence of EGC waters with reduced temperatures (from 9.14°C to 5.83°C) and salinities (from 34.99 to 33.84) as a consequence of freshwater advection south through Fram Strait in addition to local glacier and iceberg melt water inputs from Greenland (Sutherland et al., 2009). The DMn concentrations on the Greenland shelf (200 m water depth) reached >2 nM and were fairly constant below ~40 m depth, coinciding with elevated DFe values (up to 1 nM; Achterberg et al., 2018) indicating a benthic release of these elements following reductive dissolution (Burdige, 1993). Concentrations of TDMn were also elevated in the Greenland shelf waters and showed an increase near the seafloor to values of 6.83 nM, as a consequence of scavenging/precipitation of DMn diffusing out of the sediments and/or sediment resuspension (SI Figure S13). The dissolved concentrations of the redox sensitive element Co on the Greenland shelf in the EGC (0.03–0.12 nM) were lower or comparable to subsurface waters off shelf (~0.09–0.11 nM), indicating a low continental and Arctic Ocean supply with limited benthic release and/or important scavenging removal. The TDCo concentrations on the Greenland shelf were between 30% and 300% higher than DCo, indicating an important role for transfer of DCo onto particles (Moffett & Ho, 1996).

Trends in DCd and DZn along this section showed similarities to nutrients, with lower surface levels and an increase with depth. Dissolved Cd showed a pronounced difference between surface and deep water concentrations (e.g., station 13: 0.024 nM surface and 0.22 nM at 300 m). Dissolved Cu and DNi showed elevated concentrations on the Greenland shelf in the EGC, with invariable concentrations with depth and an absence of surface water depletion, likely as a result of enhanced supply and a minimal removal through biological activity.

Dissolved Pb concentrations along the section were similar to other parts of the IB and IRB, and ranged between 0.017–0.03 nM, including concentrations up to 0.024 nM in the EGC, with little depth-related variation, and >80% of Pb in the dissolved phase. The surface water concentrations of DAl ranged between ~0.9–2.8 nM with TDAl being up to 10 times higher, and deep water DAl levels increased to 7 nM on shelf and 14 nM off shelf with TDAl being several fold higher.

Clear differences are apparent between the distributions of the various elements. We used principal component analysis (PCA) with the full data set to determine relationships between various oceanographic variables and hence suggest which processes dominate observed combined trace element distributions in an overall statistical sense (Figure 8). The first principal component axis (PC1) explains 48% of the variance and represents mainly depth dependent increases in nutrients and trace elements involved in biological processes and controlled by organic matter production and remineralization, including DCd, DZn, DCu, and DNi but potentially also DPb and DAl. Phosphate and DCd correlate as does Si with both DZn and DAl, in accordance with previous studies (Bruland et al., 2014; Menzel Barraqueta et al., 2018; Middag et al., 2019; Xie et al., 2015). The PCA results also agree with elevated Pearson correlations for the relationships of DCd, DZn, DCu, and DNi with depth (r = 0.50, 0.59, 0.45, and 0.32, resp.), TON (r = 0.91, 0.51, 0.28, and 0.39, resp.), phosphate (r = 0.90, 0.58, 0.42, and 0.39, resp.), and silicic acid (r = 0.83, 0.67, 0.43, and 0.46, resp.) (SI, Table S3). Enhanced Pearson correlations were observed for the relationships of DPb and DAl with TON (r = 0.46 and 0.53, resp.), phosphate (r = 0.46 and 0.51, resp.), and silicic acid (r = 0.29 and 0.75, resp.) (SI, Table S3). While DPb and DAl distributions are known to be influenced by atmospheric inputs, sediment supply, and scavenging (Measures & Vink, 2000; Menzel Barraqueta et al., 2019; Rusiecka et al., 2018), an association of Al with diatom frustules (Menzel Barraqueta et al., 2018), and Pb with organic matter remineralization and sediment supply (Rusiecka et al., 2018) has recently been reported. A role of Mn and Fe in DPb cycling (but not DAl) is suggested by negative Pearson correlations (r = −0.45 and −0.35 for DPb with TDMn and TDFe, resp.) indicating lower DPb at elevated particulate Mn and Fe concentrations related to scavenging.

Dissolved Mn, Co and Fe are micronutrients, and in Figure 8 fall on the trajectory of the other nutrient-type elements (e.g., Cd), but less of their variance is explained by PC1, indicating that processes other than biological uptake and remineralization influenced their distributions. While these redox sensitive elements have elevated concentrations in oxygen minimum zones as a result of benthic supply (Bruland et al., 2005; Rapp et al., 2019; Schroller-Lomnitz et al., 2019), no association with low oxygen is notable in Figure 8 and their variance is not explained by the oxygen/salinity correlated PC2. As might be expected, the dissolved concentrations of Mn, Co, and Fe therefore appear to be determined by a combination of factors including supply strength, biological uptake and remineralization, characteristics and abundance of particles, and water mass age and mixing.

Plots of nutrients versus trace elements (Figures S6–S8) confirm the findings of the PCA and Pearson correlations, and show the strong relationships between Si and DZn, and TON/phosphate and DCd. The slopes of the DZn-Si (DZn-PO_4) relationship were 0.084 (0.50) for <5 μM Si (<0.75 μM PO_4) and 0.201 (2.79) for >5 μM Si (>0.75 μM PO_4), and compare fairly well with slopes of 0.14 (3.0) for waters between 57.5°N and 64°N reported by (Middag et al., 2019) for cruise GA02. Furthermore, the slope of the DNi-PO_4 relationship was 1.04 and compares well with slopes of 1.4 for N Atlantic Central Waters between 50°N and 64°N and 0.6 for North Atlantic Subpolar Mode Waters reported by (Middag et al., 2020). The slope of the DCd-PO_4 relationship was 0.217 and compares well with slopes between 0.2 and 0.24 for the waters between 50°N and 64°N for GA02 reported by (Middag et al., 2018). The DCd-PO_4 slope is indicative of surface waters and relatively young Atlantic waters with <1.3 μM PO_4 and a regression through the origin, with Indian, Pacific, and Southern Oceans sourced waters providing a steeper slope and a resulting kink at >1.3 μM PO_4 and a regression with a non-zero intercept (de Baar et al., 1994).

3.5. Trace Element Supply to Surface Waters of the IB and IRB

The transfer of trace elements to surface waters for the following sources has been estimated: (i) atmospheric inputs, (ii) winter convective supply, and (iii) diffusive fluxes, while it is assumed that the horizontal fluxes are small as the horizontal concentration gradients off shelf were relatively minor (also see Achterberg et al., 2018).

3.5.1. Atmospheric Supply

Atmospheric concentrations of soluble and total trace elements determined using direct aerosol sampling on the spring and summer cruises are presented in Tables 3 and SI Table S4, respectively. The summer cruise observations (fine and coarse fractions combined; Table 3) for soluble Al, Mn, Cu, and Ni were within the range of concentrations reported for these elements in remote North Atlantic aerosols from the AMT 18–21 cruises (soluble Al: 25–862 pmol m^{-3}, soluble Mn: 0.4–46 pmol m^{-3}, soluble Cu, 1.8–22.3 pmol m^{-3}, soluble Ni: 1.2–18.4 pmol m^{-3}), using the same leaching procedure as our study (Baker & Jickells, 2017). Soluble Zn concentrations were a little lower than those reported by Baker and Jickells (2017) (36–530 pmol m^{-3}). Aerosol concentrations in the vicinity of Iceland (between 59.1°N and 62.8°N, 20°W; CLIVAR A16) for deionized water soluble Al ranged between 70–125 pmol m^{-3}, Mn between 1.6 and 2.2 pmol m^{-3} and Pb 0.4 and 0.6 pmol m^{-3} (Buck et al., 2010) and were therefore similar to our summer cruise observations (fine and coarse fractions combined; Table 3). Reported aerosol concentrations (Shelley et al., 2018) from GEOTRACES cruise GA01 in the high-latitude North Atlantic (sample G13, 59.6°N and 38.9°W) for soluble Al (45.9 pmol m^{-3}), Ni (0.322 pmol m^{-3}), Co (0.005 pmol m^{-3}), Cd (0.002 pmol m^{-3}), and Pb (0.290 pmol m^{-3}) (25% acetic acid leach) were similar to our summer cruise observations (fine and coarse fractions combined; Table 3), but their Mn (0.133 pmol m^{-3}), Zn (0.330 pmol m^{-3}), and Cu (0.107 pmol m^{-3}) concentrations were lower than ours. Our observations for soluble trace element concentrations are therefore in reasonable agreement with literature values, while recognizing that individual observations made during cruises do not reflect the intra-annual variability of aerosol concentrations in the high-latitude North Atlantic that can be important (Prospero et al., 2012).

In some cases, soluble element concentrations in the spring non-volcanic samples (TM02-06) were up to several fold (Al, Mn, and Pb) or more than an order of magnitude (Cu and Cd) higher than their respective concentrations in the summer. In particular, the concentrations for samples TM04-06 in the IB were above background levels, probably as a result of longer-range transport of ash from the eruption, as indicated by air mass back trajectories (SI Figures S14–S16). The increases were not consistent with the proportions in which the elements were observed in samples collected under the ash plume, which could possibly be

Global Biogeochemical Cycles

10.1029/2020GB006674

Table 3
Atmospheric Trace Element Soluble Concentrations (pmol m^{-3}) During Spring and Summer 2010

	Start date	Lat.	Long.	Al		Mn		Zn		Cu	
Spring				Bulk		Bulk		Bulk		Bulk	
TM02	28/04/2010	58.39	−20.92	69.6 ± 26.7		1.67 ± 0.48		22.7 ± 4.3		60.6 ± 0.3	
TM03	29/04/2010	59.70	−30.62	190 ± 4.6		10.7 ± 0.29		5.7 ± 1.3		37.0 ± 0.2	
TM04	02/05/2010	59.98	−30.26	479 ± 8.3		9.53 ± 0.62		577 ± 130		218 ± 1.1	
TM05	05/05/2010	60.97	−22.88	425 ± 4.9		11.6 ± 0.54		14.2 ± 4.2		423 ± 2.1	
TM06	07/05/2010	62.50	−19.97	619 ± 10		10.2 ± 0.73		6.8 ± 2.1		26.2 ± 0.2	
TM07	08/05/2010	63.10	−18.75	33,586 ± 103		327 ± 9.4		193 ± 31		146 ± 1.2	
TM08	08/05/2010	63.09	−19.08	17,760 ± 109		252 ± 7.3		62 ± 19		289 ± 1.7	
TM09	09/05/2010	63.39	−21.31	1,280 ± 450		25.6 ± 4.3		<40		147 ± 1.5	
Summer				<1 μm	>1 μm	<1 μm	>1 μm	<1 μm	>1 μm	<1 μm	>1 μm
TM10	17/07/2010	60.00	−38.59	29.7 ± 3.2	28.4 ± 3.6	0.34 ± 0.06	0.38 ± 0.08	9.4 ± 3.4	<2.4	3.6 ± 0.5	0.8 ± 0.4
TM11	19/07/2010	60.72	−38.49	22.6 ± 7.5	67.9 ± 6.5	0.37 ± 0.08	2.06 ± 0.24	14.8 ± 5.4	9.7 ± 2.4	4.8 ± 0.6	6.1 ± 0.4
TM12	23/07/2010	61.19	−32.98	29.9 ± 3.8	512 ± 4	0.45 ± 0.06	1.09 ± 0.12	<9.8	<4.6	1.5 ± 0.5	1.6 ± 0.3
TM13	26/07/2010	59.42	−33.40	95.9 ± 3.7	188.8 ± 4.7	0.35 ± 0.05	1.08 ± 0.08	11.4 ± 2.4	5.0 ± 1.6	1.6 ± 0.3	1.4 ± 0.2
TM14	29/07/2010	63.41	−29.43	1948 ± 96[a]	204 ± 1.4	6.88 ± 0.34[a]	0.88 ± 0.06	27.1 ± 2.5[a]	3.1 ± 0.9	1.6 ± 0.2	0.8 ± 0.4
TM15	04/08/2010	61.18	−22.42	44.8 ± 2.6	82.2 ± 4.0	0.65 ± 0.06	0.82 ± 0.10	<8.7	<5.4	2.0 ± 0.4	1.4 ± 0.7
	Ni		Co		Cd		Pb				
	Bulk		Bulk		Bulk		Bulk				
Spring											
TM02	1.11 ± 0.10		<0.031		13.2 ± 0.34		0.31 ± 0.011				
TM03	<0.25		0.084 ± 0.007		2.35 ± 0.09		1.61 ± 0.01				
TM04	4.53 ± 0.13		0.13 ± 0.02		4.42 ± 0.17		1.14 ± 0.01				
TM05	0.96 ± 0.08		0.12 ± 0.01		4.11 ± 0.13		1.84 ± 0.01				
TM06	0.73 ± 0.14		0.13 ± 0.02		4.48 ± 0.17		1.38 ± 0.01				
TM07	<3.9		1.91 ± 0.30		142 ± 3.6		23.2 ± 0.13				
TM08	2.88 ± 0.78		1.97 ± 0.17		73.3 ± 1.9		10.6 ± 0.08				
TM09	9.3 ± 2.1		<0.60		14.0 ± 2.1		3.41 ± 0.22				
Summer	<1 μm	>1 μm	<1 μm	>1 μm	<1 μm	>1 μm	<1 μm	>1 μm			
TM10	0.38 ± 0.15	<0.11	0.086 ± 0.015	0.055 ± 0.013	0.087 ± 0.003	0.011 ± 0.002	0.85 ± 0.06	<0.07			
TM11	0.61 ± 0.95	0.88 ± 0.94	<0.050	<0.071	0.15 ± 0.005	0.11 ± 0.003	0.48 ± 0.10	0.32 ± 0.03			
TM12	0.83 ± 0.67	0.87 ± 0.36	<0.036	<0.050	0.028 ± 0.004	0.048 ± 0.003	<0.21	<0.07			
TM13	0.53 ± 0.53	0.45 ± 0.33	0.11 ± 0.01	0.124 ± 0.01	0.02 ± 0.003	0.015 ± 0.002	<0.15	<0.05			
TM14	1.47 ± 0.44	0.72 ± 0.36	0.075 ± 0.01	0.071 ± 0.01	0.12 ± 0.002	0.017 ± 0.001	<0.10	<0.04			
TM15	<0.27	0.17 ± 0.27	<0.03	<0.043	0.08 ± 0.003	0.016 ± 0.003	0.24 ± 0.06	<0.06			

Note. Spring cruise samples were collected in a single size fraction (Bulk), summer cruise samples were fractionated into particles <1 μm and >1 μm.
[a]Probable contamination. The latitudes and longitudes are the midpoints of aerosol sample collection; dates are at start point of collection. See Figure S2 (SI) for aerosol sampling map.

Table 4
Calculated Dry Deposition Fluxes (nmol m^{-2} day^{-1}) for Soluble Metals During the Spring and Summer Cruises

	Al	Mn	Zn	Cu	Ni	Co	Cd	Pb
				Spring				
TM02	42	1.0	2.0	5.2	0.096	<0.019	1.14	0.027
TM03	115	6.4	0.5	3.2	<0.018	0.051	0.20	0.139
TM04	289	5.8	49.9	18.9	0.391	0.078	0.38	0.098
TM05	257	7.0	1.2	36.5	0.083	0.074	0.35	0.159
TM06	374	6.2	0.6	2.3	<0.084	0.078	0.39	0.119
TM07	20,300	198	16.7	12.6	0.218	1.16	12.2	2.00
TM08	10,700	152	5.3	25.0	0.249	1.19	6.33	0.911
TM09	774	15.5	<2.9	12.7	0.803	<0.36	1.21	0.295
				Summer				
TM10	27	0.4	2.3	1.0	0.105	0.055	0.017	0.115
TM11	61	1.8	9.7	5.6	0.815	<0.065	0.111	0.320
TM12	445	1.0	<4.8	1.5	0.820	<0.047	0.044	<0.080
TM13	171	1.0	5.3	1.4	0.434	0.117	0.015	<0.057
TM14	344	1.4	5.0	0.9	0.744	0.068	0.024	<0.041
TM15	75	0.8	<5.4	1.3	0.167	<0.040	0.021	0.061

Note. Deposition fluxes are uncertain by a factor of 2–3 (Duce et al., 1991).

related to changing properties of ejected materials during different phases of eruption, and/or contributions of additional aerosol sources to these spring samples. Size fractionated aerosol soluble Cu, Ni, Co, and Cd concentrations for the <1 and >1 μm fractions observed during the summer cruise were approximately equal at some stations. For soluble Pb, the <1 μm fraction was ~2–6 times higher than the >1 μm fraction, and for soluble Zn between 1.5 and 9 times, as also reported by (Arimoto & Duce, 1986; Fomba et al., 2013) and related to their industrial sources from high temperature combustion processes. Concentrations of the soluble Mn fraction of <1 μm were between 1.1 and 6 times smaller than the >1 μm fraction, and for soluble Al ranging from equal to 17 times smaller, in accordance with the lithogenic nature of these elements (Arimoto & Duce, 1986; Baker & Jickells, 2017; Fomba et al., 2013).

Rates of dry deposition of soluble trace elements are presented in Table 4, and for many elements (Al, Mn, Co, Cd, and Pb) these fluxes were higher by factors of 9–113 under the Eyjafjallajökull volcanic ash plume (spring TM07-09) than for all other samples (ratios of median volcanic to median non-volcanic fluxes). The spatial extent of the direct volcanically derived input fluxes thus appeared to be restricted to waters in the vicinity of Iceland (Achterberg et al., 2013; Gudmundsson et al., 2012). Chemical analysis of Eyjafjallajökull ash collected at sea during cruise D350 indicated 7.91% Al and 0.17% Mn by weight, 173 μg g^{-1} Zn, 55.2 μg g^{-1} Ni, and 4.53 μg g^{-1} Pb (sample EYJ 04; SI, Table S5; data from Achterberg et al., 2013), consistent with other reports for this material (Gislason et al., 2011) who additionally report on Cu (35 μg g^{-1}) and Co (33 μg g^{-1}). The solubilities of the aerosol samples (defined as the ratio of soluble to total element concentration) affected by the volcanic emissions were lower compared to other samples (SI, Table S6). However, it should be noted that in some cases (particularly for Ni) total element concentrations were below detection limit and only minimum values for solubility could be determined. For example, the median solubilities of the ash plume samples were 0.92% for Al and 0.96% for Mn, compared to medians of 8.8% and 27% respectively for the other samples. Similar patterns in solubility between the ash and non-volcanic samples were apparent for the other trace elements, with the possible exception of Cd (see SI, Table S6). The soluble trace element inputs to the surface ocean related to ash deposition are likely dominated by a highly soluble salt layer (up to 300 nm) of metal halides and sulfates formed on the ash particles within the volcanic plumes and during their onward transport through coagulation with aerosol (i.e., SO_4) and the condensation of acidic gases (i.e., SO_2, HCl, and HF) (Duggen et al., 2010; Gislason et al., 2011). The main ash fraction had a mean grain size of 123 μm and would have settled through a 30 m mixed layer in ~1.5 hr (Achterberg et al., 2013), and therefore, the short residence time and the relatively low elemental solubilities of the ash limit the inputs for a range of soluble elements including Co, Cd, Cu, Ni, and Pb related to the eruption of the Eyjafjallajökull volcano. This is also evidenced by a lack of elevated surface water concentrations for these elements in the vicinity of Iceland during the spring cruise (Figure 2).

3.5.2. Diffusive Vertical Fluxes

Diffusive dissolved trace element fluxes were determined during summer 2010 at 21 stations, and the data compiled for annual fluxes in the IB and IRB (Table 5). In general, there was widespread variability in the direction and magnitude of diffusive trace element fluxes, with fluxes both into and out of the mixed layer estimated. The annual diffusive fluxes for the IB and IRB were similar for dissolved Cd and Pb, with three times higher Co fluxes in the IRB and two times lower Mn fluxes in the IRB compared to the IB. The annual fluxes had opposite directions in the IB and IRB for dissolved Ni, Zn, Cu, and Al. The variability in annual diffusive fluxes for the various elements was a function of near-surface elemental gradients, which is related to elemental removal by biological uptake and scavenging, and supply by organic matter remineralization at the base of the mixed layer. Consequently, the overall picture of diffusive elemental supply to surface waters in our study area during summer is variable with no clear geographical or regional patterns.

3.5.3. Convective Supply

There is a paucity of data on the winter convective supply of trace elements to surface waters of the high-latitude North Atlantic. Annual convective DFe inputs have been reported for the IB

Table 5
Annual Convective, Diffusive, and Atmospheric Trace Element Fluxes, With Their Uncertainties

	DCo	DMn	DNi	DCd	DPb	DZn	DCu	DAl
				Iceland Basin				
Annual diffusive flux (μmol m^{-2} $year^{-1}$)		2.07 ± 0.25	−0.39 ± 0.94			−0.89 ± 1.44	−0.78 ± 0	12.2 ± 0.13
Annual diffusive flux (nmol m^{-2} $year^{-1}$)	55.6 ± 22.4			1,198 ± 56.1	55.6 ± 24.6			
Convective flux (mmol m^{-2} $year^{-1}$)		0.03 ± 0.01	0.18 ± 0.02			0.04 ± 0.02	0.05 ± 0.01	0.29 ± 0.05
Convective flux (μmol m^{-2} $year^{-1}$)	3.98 ± 0.36			8.85 ± 0.7	1.37 ± 0.18			
Atmospheric flux (μmol m^{-2} $year^{-1}$)	0.011 (0.006–0.022)	0.28 (0.14–0.56)	0.06 (0.03–0.12)	0.008 (0.004–0.016)	0.012 (0.006–0.024)	1.46 (0.73–2.92)	0.48 (0.24–0.96)	27.3 (13.7–54.6)
Diffusive flux as % convective flux	**1.40 ± 0.58**	**6.40 ± 2.26**	**−0.22 ± 0.53**	**13.5 ± 1.24**	**4.05 ± 1.86**	**−2.43 ± 4.11**	**−1.55 ± 0.93**	**4.24 ± 0.73**
Atmospheric flux as % convective + diffusive fluxes	**0.27 ± 0.34**	**0.81 ± 1.04**	**0.03 ± 0.04**	**0.08 ± 0.12**	**0.84 ± 0.64**	**4.10 ± 3.70**	**0.98 ± 0.94**	**9.11 ± 7.01**
				Irminger Basin				
Annual diffusive flux (μmol m^{-2} $year^{-1}$)		1.11 ± 1.33	0.82 ± 1.39			2.20 ± 2.1	0.80 ± 0.43	−1.04 ± 2.41
Annual diffusive flux (nmol m^{-2} $year^{-1}$)	184 ± 48.6			706 ± 321	46.7 ± 52.2			
Convective flux (mmol m^{-2} $year^{-1}$)		0.03 ± 0.001	0.20 ± 0.003			0.04 ± 0.01	0.06 ± 0.003	0.17 ± 0.004
Convective flux (μmol m^{-2} $year^{-1}$)	4.18 ± 0.03			10.3 ± 1.03	1.55 ± 0.03			
Atmospheric flux (μmol m^{-2} $year^{-1}$)	0.022 (0.011–0.044)	0.38 (0.19–0.76)	0.19 (0.1–0.38)	0.014 (0.007–0.028)	0.041 (0.02–0.084)	1.86 (0.93–3.66)	0.71 (0.35–1.42)	68.4 (34.2–137)
Diffusive flux as % convective flux	**4.40 ± 1.16**	**4.08 ± 4.89**	**0.40 ± 0.67**	**6.87 ± 3.20**	**3.02 ± 3.36**	**5.16 ± 5.09**	**1.34 ± 0.72**	**−0.63 ± 1.46**
Atmospheric flux as % convective + diffusive fluxes	**0.50 ± 0.63**	**1.34 ± 1.67**	**0.09 ± 0.06**	**0.13 ± 0.14**	**2.57 ± 2.01**	**4.15 ± 3.27**	**1.16 ± 1.75**	**41.7 ± 31.3**

Note. Diffusive and atmospheric fluxes derived from observations made during summer cruise. The convective flux uncertainties are based on the use of mean and standard deviation estimates of the metal concentrations at the winter mixed layer depth of the respective basin. The uncertainties for the atmospheric fluxes are indicated as a range in parentheses, with the range being the relevant flux value divided by, and multiplied by, an uncertainty of factor 2 in deposition velocity (Duce et al., 1991). The variability in atmospheric fluxes of the various elements is less than 20% for the samples collected in the respective IB and IRB, and therefore, a more realistic flux range is presented based on the deposition velocity uncertainty. Entries in normal font are fluxes, and entries in bold font are percentages.

(Forryan et al., 2012), and DFe and DAl for our cruise program covering a wider geographical region, including both the IB and IRB (Achterberg et al., 2018; Painter et al., 2014), and using a similar technique to Forryan et al. (2012). Here we employed the same approach, and determined convective trace elements inputs to surface waters of the IB and IRB during winter 2010. The convective supply of dissolved Co, Mn, Ni, Cd, Cu, Pb, Zn, and Al all showed positive values (Table 5), indicating that subsurface stocks with elevated concentrations were accessed during deep winter mixing, which resulted in a replenishment of depleted surface water stocks. Consequently, the winter mixing was deeper than for example the ferricline or nutricline (Rigby et al., 2020; Tagliabue et al., 2014). This was also the case for the scavenged-type element Mn, which in many ocean regions shows vertical profiles with a depletion with depth due to scavenging, resulting in a dilution by winter mixing of surface water stocks in the Atlantic between 40°S and 40°N (Rigby et al., 2020). The positive Mn supply through convective mixing was related to the surface ocean depletion observed for DMn in this study (Figure 4) which is then resupplied during winter from deeper water pools. The convective supply rates were remarkably similar for all the elements between the IB and IRB, with typically less than 10% difference, despite differences in deep winter mixing depths (IB 350 m, IRB 200 m). This is in contrast to convective DFe supply, which was nearly four times higher in the IB compared to the IRB (Painter et al., 2014), with the difference related to differences between DFe profiles. Winter mixing depths also change on an interannual basis, with reported depths for the IB of 600 m previously used (Forryan et al., 2012) for DFe convective supply calculations for winter 2007.

The magnitude of estimated convective fluxes indicated that diffusive supply of trace elements was a small supply term to the surface mixed layer relative to convective mixing, ranging from −2.43% for DZn to 13.5% for DCd in the IB to −0.63% for DAl to 6.87% for DCd in the IRB (Table 5). The atmospheric fluxes relative to the combined convective + diffusive fluxes were largest for DAl (9.1% in IB, and 42% in IRB) which has a known atmospheric supply route (Menzel Barraqueta et al., 2019). For the other elements, the atmospheric fluxes were relatively small and less than 4.2% for DZn and 0.13% for DCd, and even less than 2.57% for DPb which has a known atmospheric supply route to the oceans (Boyle et al., 1986, 2014). The observed atmospheric inputs and diffusive vertical fluxes are subject to temporal and spatial variability and have an inherent uncertainty, but overall indicate that these fluxes of dissolved trace elements into the IB and IRB are significantly lower than the fluxes associated with winter mixing.

Convection thus played a dominant role in the supply of dissolved elements to the surface waters, with total supply ratios (relative to P) that were very similar in both basins (Table 2), in agreement with the similarities between supply rates through convection (see above and Table 5). The supply ratios of the various elements are determined by the shape of their vertical profiles and the depth of winter mixing in the respective basin. As a consequence, the trace element: P supply ratios for Zn, Cu, Mn, and Fe were similar and ~4 times higher than Cd, approximately tenfold higher than Co, ~25–30 times higher than Pb, but ~4–7 times lower than Al (Table 2). As mentioned above, the Fe supply ratio was more than 3 times higher in the IB than the IRB, and related to differences in vertical DFe profiles (Achterberg et al., 2018). To first order, total elemental supply ratios were comparable to the apparent removal ratios we calculated between spring and summer (Table 2), suggesting an overall balance between multi-element supply and biologically mediated export stoichiometry in the region. The reasonable agreement occurred despite the different time windows used for the ratio calculations (spring to summer concentration differences for removal ratio and winter convection for supply ratio). Supply ratios were however generally higher than removal ratios relative to P over the sampled periods (Table 2), with some variability between the trace metals. The overall tendency for supply ratios to exceed removal from spring to summer may reflect preferential remineralization of the trace metals in these surface waters relative to P (Boyd et al., 2017; Rafter et al., 2017). Further elevated supply ratios relative to removal for the redox sensitive and scavenged-type elements (Fe, Mn, Co, and Pb) may then be related to additional dissolved-particle phase processes (colloid formation and scavenging without coinciding P removal, taking place year-round) which will ultimately influence both surface retention (Boyd et al., 2017) and subsurface profiles (Figure 4) and hence convective re-supply to the surface.

4. Conclusions

This study provides a unique picture of changes from spring to summer in trace element concentrations in the high-latitude North Atlantic, a region with pronounced spring blooms and deep water formation. The eruption in spring 2010 of the Eyjafjallajökull volcano resulted in pronounced increases in Al, Mn, and Zn in surface waters near Iceland, with concentrations returning to more typical values for the region in summer.

Convective mixing formed the dominant supply mechanism of multiple trace elements to the surface waters, with elemental ratios (relative to P) of convective supply similar to ratios of likely biologically dominated removal. The convective fluxes of bio-essential elements and nutrients would be expected influence magnitude and duration of the high-latitude North Atlantic spring bloom, setting an upper bound on export potential from the system (Forryan et al., 2012; Nielsdottir et al., 2009; Painter et al., 2014), although additional control by light availability and loss process due to zooplankton grazing could potentially result in this upper bound not being achieved. Interannual variability in the strength of the convective supply might thus influence biological productivity in the region. Over the Mid-Atlantic Ridge, maximum winter mixing depths along 60°N do not usually exceed 300 m (de Boyer Montégut et al., 2004), in agreement with depths down to 400 m as observed at moorings in the central IB (de Jong et al., 2012); however, extreme mixing depths of 1 km are possible in cold winters. Therefore, during cold winters the trace element supply to surface waters by convective mixing will be further enhanced. Atmospheric inputs are often considered to form an important source of bio-essential elements to the surface ocean (Duce et al., 1991). However, we show that atmospheric and also diffusive fluxes were low compared to convective fluxes in the high-latitude North Atlantic, but nevertheless they provide a sustained trace element supply during the summer period after the winter mixing derived elements may have been depleted.

In contrast, ocean warming is considered to result in upper ocean density stratification. A significant strengthening of stratification (3.3–6.1% increase of mean stratification) has been observed in ~40% of the global ocean since the 1960s (Yamaguchi & Suga, 2019). A shoaling of the maximum depths of winter mixing is projected in climate models as a consequence of the increased stratification (Capotondi et al., 2012). For our study region, assuming it behaves as the global mean, this would likely result in a reduced supply of nutrients and trace elements, and therefore a reduction in productivity and potentially carbon export. Projections for the North Atlantic subpolar gyre indicated that with a 20% reduction in maximum deep winter mixing depth, a reduced supply of all elements will occur, with the exception of scavenged-type elements, where a reduced dilution of elevated surface ocean stocks might result (Rigby et al., 2020).

Upper ocean stratification is also considered to reduce the transfer of trace elements and nutrients from the deep ocean to the surface mixed layer through upwelling and diapycnal diffusion, as the barrier to transfer across the main thermocline will strengthen (Yamaguchi & Suga, 2019). A reduced advective and diffusive supply of (micro-)nutrients to the surface mixed layer in the subpolar North Atlantic will further enhance the relative importance of seasonal convective mixing, provided that the (micro-)nutrient-clines remain at shallower depths than the maximum winter MLD. Future Icelandic volcanic eruptions could thus have a larger relative impact than presented here for the same deposition magnitude.

Conflict of Interest

The authors declare no competing interests.

Data Availability Statement

Data are held at the British Oceanographic Data Centre (http://www.bodc.ac.uk/).

Acknowledgments
We thank Guantian Li for the TDAl analysis. We thank all the scientists and crew members on IBIS cruises D350/351/354 (RRS *Discovery*, 1962–2012, NERC). We acknowledge M. Stinchcombe for technical support. This work was funded by NERC (NE/E006833/1, E. P. A. and C. M. M.) and GEOMAR Helmholtz Centre for Ocean Research Kiel.

References

Achterberg, E. P., Holland, T. W., Bowie, A. R., Mantoura, R. F. C., & Worsfold, P. J. (2001). Determination of iron in seawater. *Analytica Chimica Acta*, *442*(1), 1–14. https://doi.org/10.1016/S0003-2670(01)01091-1

Achterberg, E. P., Moore, C. M., Henson, S. A., Steigenberger, S., Stohl, A., Eckhardt, S., et al. (2013). Natural iron fertilization by the Eyjafjallajökull volcanic eruption. *Geophysical Research Letters*, *40*, 921–926. https://doi.org/10.1002/grl.50221

Achterberg, E. P., Steigenberger, S., Marsay, C. M., LeMoigne, F. A., Painter, S. C., Baker, A. R., et al. (2018). Iron biogeochemistry in the high latitude North Atlantic Ocean. *Scientific Reports*, *8*, 1283. https://doi.org/10.1038/s41598-018-19472-1

Arimoto, R., & Duce, R. A. (1986). Dry deposition models and the air/sea exchange of trace elements. *Journal of Geophysical Research*, *91*(D2), 2787–2792. https://doi.org/10.1029/JD091iD02p02787

Bacon, S., Reverdin, G., Rigor, I. G., & Snaith, H. M. (2002). A freshwater jet on the east Greenland shelf. *Journal of Geophysical Research*, *107*(C7), 3068. https://doi.org/10.1029/2001JC000935

Baker, A. R., & Jickells, T. D. (2017). Atmospheric deposition of soluble trace elements along the Atlantic Meridional Transect (AMT). *Progress in Oceanography*, *158*, 41–51. https://doi.org/10.1016/j.pocean.2016.10.002

Baker, A. R., Weston, K., Kelly, S. D., Voss, M., Streu, P., & Cape, J. N. (2007). Dry and wet deposition of nutrients from the tropical Atlantic atmosphere: Links to primary productivity and nitrogen fixation. *Deep-Sea Research Part I: Oceanographic Research Papers*, *54*(10), 1704–1720. https://doi.org/10.1016/j.dsr.2007.07.001

Birchill, A. J., Hartner, N. T., Kunde, K., Siemering, B., Daniels, C., González-Santana, D., et al. (2019). The eastern extent of seasonal iron limitation in the high latitude North Atlantic Ocean. *Scientific Reports*, *9*, 1435. https://doi.org/10.1038/s41598-018-37436-3

Bower, A. S., le Cann, B., Rossby, T., Zenk, W., Gould, J., Speer, K., et al. (2002). Directly measured mid-depth circulation in the northeastern North Atlantic Ocean. *Nature*, *419*(6907), 603–607. https://doi.org/10.1038/nature01078

Boyd, P., Ellwood, M., Tagliabue, A., & Twining, B. S. (2017). Biotic and abiotic retention, recycling and remineralization of metals in the ocean. *Nature Geoscience*, *10*(3), 167–173. https://doi.org/10.1038/ngeo2876

Boyd, P. W., Jickells, T., Law, C. S., Blain, S., Boyle, E. A., Buesseler, K. O., et al. (2007). Mesoscale iron enrichment experiments 1993–2005: Synthesis and future directions. *Science*, *315*(5812), 612–617. https://doi.org/10.1126/science.1131669

Boyle, E., Lee, J.-M., Echegoyen, Y., Noble, A., Moos, S., Carrasco, G., et al. (2014). Anthropogenic lead emissions in the ocean: The evolving global experiment. *Oceanography*, *27*(1), 69–75. https://doi.org/10.5670/oceanog.2014.10

Boyle, E. A., Chapnick, S. D., Shen, G. T., & Bacon, M. P. (1986). Temporal variability of lead in the western North Atlantic. *Journal of Geophysical Research*, *91*(C7), 8573–8593. https://doi.org/10.1029/JC091iC07p08573

Boyle, E. A., Sclater, F. R., & Edmond, J. M. (1977). The distribution of dissolved copper in the Pacific. *Earth and Planetary Science Letters*, *37*(1), 38–54. https://doi.org/10.1016/0012-821X(77)90144-3

Bridgestock, L., van de Flierdt, T., Rehkämper, M., Paul, M., Middag, R., Milne, A., et al. (2016). Return of naturally sourced Pb to Atlantic surface waters. *Nature Communications*, *7*, 12921. https://doi.org/10.1038/ncomms12921

Brix, H., Gruber, N., Karl, D. M., & Bates, N. R. (2006). On the relationships between primary, net community, and export production in subtropical gyres. *Deep-Sea Research Part II: Topical Studies in Oceanography*, *53*(5–7), 698–717. https://doi.org/10.1016/j.dsr2.2006.01.024

Broecker, W. S. (1991). The great ocean conveyor. *Oceanography*, *4*(2), 79–89. https://doi.org/10.5670/oceanog.1991.07

Brown, M. T., & Bruland, K. W. (2008). An improved flow-injection analysis method for the determination of dissolved aluminum in seawater. *Limnology and Oceanography*, *6*, 87–95.

Browning, T. J., Al-Hashem, A. A., Hopwood, M. J., Engel, A., Wakefield, E. D., & Achterberg, E. P. (2019). Nutrient regulation of late spring phytoplankton blooms in the midlatitude North Atlantic. *Limnology and Oceanography*, *65*(6), 1136–1148. https://doi.org/10.1002/lno.11376

Bruland, K., & Franks, R. P. (1983). Mn, Ni, Cu, Zn and Cd in the Western North Atlantic. In C. S. Wong, E. A. Boyle, K. W. Bruland, J. D. Burton, E. D. Goldberg (Eds.), *Trace metals in seawater* (pp. 395–414). New York: Plenum Press.

Bruland, K. W., & Lohan, M. C. (2004). Controls on trace metals in seawater. In H. Elderfield (Ed.), *Treatise on geochemistry* (pp. 23–49). London: Elsevier.

Bruland, K. W., Middag, R., & Lohan, M. C. (2014). Controls of trace metals in seawater. *Treatise on Geochemistry*, 19–51. https://doi.org/10.1016/B978-0-08-095975-7.00602-1

Bruland, K. W., Rue, E. L., Smith, G. J., & Ditullio, G. R. (2005). Iron, macronutrients and diatom blooms in the Peru upwelling regime: Brown and blue waters of Peru. *Marine Chemistry*, *93*(2-4), 81–103. https://doi.org/10.1016/j.marchem.2004.06.011

Buck, C. S., Landing, W. M., Resing, J. A., & Measures, C. I. (2010). The solubility and deposition of aerosol Fe and other trace elements in the North Atlantic Ocean: Observations from the A16N CLIVAR/CO_2 repeat hydrography section. *Marine Chemistry*, *120*(1–4), 57–70. https://doi.org/10.1016/j.marchem.2008.08.003

Burdige, D. J. (1993). The biogeochemistry of manganese and iron reduction in marine sediments. *Earth-Science Reviews*, *35*(3), 249–284. https://doi.org/10.1016/0012-8252(93)90040-E

Capotondi, A., Alexander, M. A., Bond, N. A., Curchitser, E. N., & Scott, J. D. (2012). Enhanced upper ocean stratification with climate change in the CMIP3 models. *Journal of Geophysical Research*, *117*, C04031. https://doi.org/10.1029/2011JC007409

Chester, R., Murphy, K. J. T., Lin, F. J., Berry, A. S., Bradshaw, G. A., & Corcoran, P. A. (1993). Factors controlling the solubilities of trace-metals from nonremote aerosols deposited to the sea-surface by the dry deposition mode. *Marine Chemistry*, *42*(2), 107–126. https://doi.org/10.1016/0304-4203(93)90241-F

Clément, L., Thurnherr, A. M., & St. Laurent, L. C. (2017). Turbulent mixing in a deep fracture zone on the mid-Atlantic ridge. *Journal of Physical Oceanography*, *47*(8), 1873–1896. https://doi.org/10.1175/JPO-D-16-0264.1

de Baar, H. J. W., Saager, P. M., Nolting, R. F., & van der Meer, J. (1994). Cadmium versus phosphate in the world ocean. *Marine Chemistry*, *46*(3), 261–281. https://doi.org/10.1016/0304-4203(94)90082-5

de Boyer Montégut, C., Madec, G., Fischer, A. S., Lazar, A., & Iudicone, D. (2004). Mixed layer depth over the global ocean: An examination of profile data and a profile-based climatology. *Journal of Geophysical Research*, *109*, C12003. https://doi.org/10.1029/2004JC002378

de Jong, M. F., van Aken, H. M., Vage, K., & Pickart, R. S. (2012). Convective mixing in the central Irminger Sea: 2002 to 2010. *Deep-Sea Research Part I: Oceanographic Research Papers*, *63*, 36–51. https://doi.org/10.1016/j.dsr.2012.01.003

Duce, R. A., Liss, P. S., Merrill, J. T., Atlas, E. L., Buat-Menard, P., Hicks, B. B., et al. (1991). The atmospheric input of trace species to the world ocean. *Global Biogeochemical Cycles*, *5*(3), 193–259. https://doi.org/10.1029/91GB01778

Duggen, S., Croot, P., Schacht, U., & Hoffmann, L. (2007). Subduction zone volcanic ash can fertilize the surface ocean and stimulate phytoplankton growth: Evidence from biogeochemical experiments and satellite data. *Geophysical Research Letters*, *34*, L01612. https://doi.org/10.1029/2006GL027522

Duggen, S., Olgun, N., Croot, P., Hoffmann, L., Dietze, H., Delmelle, P., & Teschner, C. (2010). The role of airborne volcanic ash for the surface ocean biogeochemical iron-cycle: A review. *Biogeosciences*, *7*(3), 827–844. Available at: http://www.biogeosciences.net/7/827/2010/, https://doi.org/10.5194/bg-7-827-2010

Echegoyen, Y., Boyle, E. A., Lee, J.-M., Gamo, T., Obata, H., & Norisuye, K. (2014). Recent distribution of lead in the Indian Ocean reflects the impact of regional emissions. *Proceedings of the National Academy of Sciences of the United States of America*, *111*(43), 15,328–15,331. https://doi.org/10.1073/pnas.1417370111

Fitzsimmons, J. N., John, S. G., Marsay, C. M., Hoffman, C. L., Nicholas, S. L., Toner, B. M., et al. (2017). Iron persistence in a distal hydrothermal plume supported by dissolved-particulate exchange. *Nature Geoscience*, *10*(3), 195–201. https://doi.org/10.1038/ngeo2900

Fomba, K. W., Müller, K., van Pinxteren, D., & Herrmann, H. (2013). Aerosol size-resolved trace metal composition in remote northern tropical Atlantic marine environment: Case study Cape Verde islands. *Atmospheric Chemistry and Physics*, *13*(9), 4801–4814. https://doi.org/10.5194/acp-13-4801-2013

Forryan, A., Martin, A. P., Srokosz, M. A., Popova, E. E., Painter, S. C., & Stinchcombe, M. C. (2012). Turbulent nutrient fluxes in the Iceland Basin. *Deep-Sea Research Part I: Oceanographic Research Papers*, *63*, 20–35. https://doi.org/10.1016/j.dsr.2011.12.006

Ganzeveld, L., Lelieveld, J., & Roelofs, G.-J. (1998). A dry deposition parameterization for sulfur oxides in a chemistry and general circulation model. *Journal of Geophysical Research*, *103*(D5), 5679–5694. https://doi.org/10.1029/97JD03077

Gehlen, M., Beck, L., Calas, G., Flank, A.-M., Van Bennekom, A. J., & Van Beusekom, J. E. E. (2002). Unraveling the atomic structure of biogenic silica: Evidence of the structural association of Al and Si in diatom frustules. *Geochimica et Cosmochimica Acta*, *66*(9), 1601–1609. https://doi.org/10.1016/S0016-7037(01)00877-8

Giering, S. L. C., Sanders, R., Achterberg, E. P., Steigenberger, S., Poulto, A., & Mayor, D. J. (2012). Iron recycling by mesozooplankton supports phytoplankton growth in the Irminger Basin. *Geophysical Research Letters*, *39*, L12608. https://doi.org/10.1029/2012GL051776

Gislason, S. R., Hassenkam, T., Nedel, S., Bovet, N., Eiriksdottir, E. S., Alfredsson, H. A., et al. (2011). Characterization of Eyjafjallajökull volcanic ash particles and a protocol for rapid risk assessment. *Proceedings of the National Academy of Sciences*, *108*(18), 7307–7312. https://doi.org/10.1073/pnas.1015053108

Grasshoff, K., Ehrhardt, M., & Kremling, K. (1983). *Methods of seawater analysis*. (2nd ed., pp. 1–419). New York: Verlag Chemie Weinheim.

Graziano, L. M., Geider, R. J., Li, W. K. W., & Olaizola, M. (1996). Nitrogen limitation of North Atlantic phytoplankton: Analysis of physiological condition in nutrient enrichment experiments. *Aquatic Microbial Ecology*, *11*, 53–64. https://doi.org/10.3354/ame011053

Gudmundsson, M. T., Thordarson, T., Höskuldsson, Á., Larsen, G., Björnsson, H., Prata, F. J., et al. (2012). Ash generation and distribution from the April-May 2010 eruption of Eyjafjallajökull, Iceland. *Nature Scientific Reports*, *2*, 572. https://doi.org/10.1038/srep00572

Hamme, R. C., Webley, P. W., Crawford, W. R., Whitney, F. A., DeGrandpre, M. D., Emerson, S. R., et al. (2010). Volcanic ash fuels anomalous plankton bloom in subarctic northeast Pacific. *Geophysical Research Letters*, *37*, L19604. https://doi.org/10.1029/2010GL044629

Henderson, G. M., Anderson, R. F., Adkins, J., Andersson, P., Eisenhauer, A., Frank, M., & Oschlies, A. (2007). GEOTRACES—An international study of the global marine biogeochemical cycles of trace elements and their isotopes. *Chemie der Erde-Geochemistry*, *67*, 85–131.

Hydes, D. J., Aoyama, M., Aminot, A., Bakker, K., Becker, S., Coverly, S., et al. (2010). Determination of dissolved nutrients (N, P, SI) in seawater with high precision and inter-comparability using gas-segmented continuous flow analysers, In *Global Repeat Hydrography Program Manual, IOCCP Report No. 14., ICPO Publication Series No., 134, Version 1*. Paris.

Kadko, D. (1993). An assessment of the effect of chemical scavenging within submarine hydrothermal plumes upon ocean geochemistry. *Earth and Planetary Science Letters*, *120*(3–4), 361–374. https://doi.org/10.1016/0012-821X(93)90250-D

Laès, A., Blain, S., Laan, P., Ussher, S. J., Achterberg, E. P., Tréguer, P., & de Baar, H. J. W. (2007). Sources and transport of dissolved iron and manganese along the continental margin of the Bay of Biscay. *Biogeosciences*, *4*(2), 181–194. https://doi.org/10.5194/bg-4-181-2007

Le Moigne, F. A. C., Moore, C. M., Sanders, R. J., Villa-Alfageme, M., Steigenberger, S., & Achterberg, E. P. (2014). Sequestration efficiency in the iron-limited North Atlantic: Implications for iron supply mode to fertilized blooms. *Geophysical Research Letters*, *41*, 4619–4627. https://doi.org/10.1002/2014GL060308

Lévy, M., Ferrari, R., Franks, P. J. S., Martin, A. P., & Rivière, P. (2012). Bringing physics to life at the submesoscale. *Geophysical Research Letters*, *39*, L14602. https://doi.org/10.1029/2012GL052756

Lin, I. I., Hu, C., Li, Y.-H., Ho, T.-Y., Fischer, T. P., Wong, G. T. F., et al. (2011). Fertilization potential of volcanic dust in the low-nutrient low-chlorophyll western North Pacific subtropical gyre: Satellite evidence and laboratory study. *Global Biogeochemical Cycles*, *25*, GB1006. https://doi.org/10.1029/2009GB003758

Little, S. H., Archer, C., Milne, A., Schlosser, C., Achterberg, E. P., Lohan, M. C., & Vance, D. (2018). Paired dissolved and particulate phase Cu isotope distributions in the South Atlantic. *Chemical Geology*, *502*, 29–43. https://doi.org/10.1016/j.chemgeo.2018.07.022

Martin, J. H. (1991). Iron, Liebig's law, and the greenhouse. *Oceanography*, *4*, 53–55.

Martin, J. H., Fitzwater, S. E., Gordon, R. M., Hunter, C. N., & Tanner, S. J. (1993). Iron, primary production and carbon-nitrogen flux studies during the JGOFS North Atlantic Bloom experiment. *Deep-Sea Research Part II: Topical Studies in Oceanography*, *40*, 115–134.

Measures, C., Hatta, M., Fitzsimmons, J., & Morton, P. (2015). Dissolved Al in the zonal N Atlantic section of the US GEOTRACES 2010/2011 cruises and the importance of hydrothermal inputs. *Deep-Sea Research Part II: Topical Studies in Oceanography*, *116*, 176–186. https://doi.org/10.1016/J.DSR2.2014.07.006

Measures, C. I., Landing, W. M., Brown, M. T., & Buck, C. S. (2008). High-resolution Al and Fe data from the Atlantic Ocean CLIVAR-CO_2 repeat hydrography A16N transect: Extensive linkages between atmospheric dust and upper ocean geochemistry. *Global Biogeochemical Cycles*, *22*, GB1005. https://doi.org/10.1029/2007GB003042

Measures, C. I., & Vink, S. (2000). On the use of dissolved aluminium in surface waters to estimate dust deposition to the ocean. *Global Biogeochemical Cycles*, *14*(1), 317–327. https://doi.org/10.1029/1999GB001188

Menzel Barraqueta, J.-L., Klar, J. K., Gledhill, M., Schlosser, C., Shelley, R., Planquette, H. F., et al. (2019). Atmospheric deposition fluxes over the Atlantic Ocean: A GEOTRACES case study. *Biogeosciences*, *16*(7), 1525–1542. https://doi.org/10.5194/bg-16-1525-2019

Menzel Barraqueta, J.-L., Schlosser, C., Planquette, H., Gourain, A., Cheize, M., Boutorh, J., et al. (2018). Aluminium in the North Atlantic Ocean and the Labrador Sea (GEOTRACES GA01 section): Roles of continental inputs and biogenic particle removal. *Biogeosciences*, *15*(16), 5271–5286. https://doi.org/10.5194/bg-15-5271-2018

Middag, R., de Baar, H. J. W., & Bruland, K. W. (2019). The relationships between dissolved zinc and major nutrients phosphate and silicate along the GEOTRACES GA02 transect in the West Atlantic Ocean. *Global Biogeochemical Cycles*, *33*, 63–84. https://doi.org/10.1029/2018GB006034

Middag, R., de Baar, H. J. W., Bruland, K. W., & van Heuven, S. M. A. C. (2020). The distribution of nickel in the West-Atlantic Ocean, its relationship with phosphate and a comparison to cadmium and zinc. *Frontiers in Marine Science*, *7*, 105. https://doi.org/10.3389/fmars.2020.00105

Middag, R., van Heuven, S. M. A. C., Bruland, K. W., & de Baar, H. J. W. (2018). The relationship between cadmium and phosphate in the Atlantic Ocean unravelled. *Earth and Planetary Science Letters*, *492*, 79–88. https://doi.org/10.1016/j.epsl.2018.03.046

Milne, A., Schlosser, C., Wake, B. D., Achterberg, E. P., Chance, R., Baker, A. R., et al. (2017). Particulate phases are key in controlling dissolved iron concentrations in the (sub)tropical North Atlantic. *Geophysical Research Letters*, *44*, 2377–2387. https://doi.org/10.1002/2016GL072314

Moffett, J. W., & Ho, J. (1996). Oxidation of cobalt and manganese in seawater via a common microbially catalyzed pathway. *Geochimica et Cosmochimica Acta*, *60*(18), 3415–3424. https://doi.org/10.1016/0016-7037(96)00176-7

Moore, C. M., Mills, M. M., Milne, A., Langlois, R., Achterberg, E. P., Lochte, K., et al. (2006). Iron limits primary productivity during spring bloom development in the central North Atlantic. *Global Change Biology*, *12*(4), 626–634. https://doi.org/10.1111/j.1365-2486.2006.01122.x

Morel, F. M. M., & Price, N. M. (2003). The biogeochemical cycles of trace metals in the oceans. *Science*, *300*, 944–947.

Nelson, D. M., Brzezinski, M. A., Sigmon, D. E., & Franck, V. M. (2001). A seasonal progression of Si limitation in the Pacific sector of the Southern Ocean. *Deep-Sea Research Part II: Topical Studies in Oceanography*, *48*, 3973–3995. https://doi.org/10.1016/S0967-0645(01)00076-5

Nielsdottir, M. C., Moore, C. M., Sanders, R., Hinz, D. J., & Achterberg, E. P. (2009). Iron limitation of the postbloom phytoplankton communities in the Iceland Basin. *Global Biogeochemical Cycles*, *23*, GB3001. https://doi.org/10.1029/2008GB003410

Noble, A. E., Echegoyen-Sanz, Y., Boyle, E. A., Ohnemus, D. C., Lam, P. J., Kayser, R., et al. (2015). Dynamic variability of dissolved Pb and Pb isotope composition from the U.S. North Atlantic GEOTRACES transect. *Deep-Sea Research Part II: Topical Studies in Oceanography*, *116*, 208–225. https://doi.org/10.1016/J.DSR2.2014.11.011

Obata, H., Karatani, H., & Nakayama, E. (1993). Automated determination of iron in seawater by chelating resin concentration and chemiluminescence detection. *Analytical Chemistry*, *65*(11), 1524–1528. https://doi.org/10.1021/ac00059a007

Olsen, A., Brown, K. R., Chierici, M., Johannessen, T., & Neill, C. (2008). Sea-surface CO_2 fugacity in the subpolar North Atlantic. *Biogeosciences*, *5*(2), 535–547. https://doi.org/10.5194/bg-5-535-2008

Orians, K. J., & Bruland, K. W. (1986). The biogeochemistry of aluminum in the Pacific Ocean. *Earth and Planetary Science Letters*, *78*(4), 397–410. https://doi.org/10.1016/0012-821X(86)90006-3

Painter, S. C., Henson, S. A., Forryan, A., Steigenberger, S., Klar, J., Stinchcombe, M. C., et al. (2014). An assessment of the vertical diffusive flux of iron and other nutrients to the surface waters of the subpolar North Atlantic Ocean. *Biogeosciences*, *11*(8), 2113–2130. https://doi.org/10.5194/bg-11-2113-2014

Pickart, R. S., Straneo, F., & Moore, G. W. K. (2003). Is Labrador Sea water formed in the Irminger basin? *Deep-Sea Research Part I: Oceanographic Research Papers*, *50*(1), 23–52. https://doi.org/10.1016/S0967-0637(02)00134-6

Prospero, J. M., Bullard, J. E., & Hodgkins, R. (2012). High-latitude dust over the North Atlantic: Inputs from Icelandic Proglacial dust storms. *Science*, *335*(6072), 1078–1082. https://doi.org/10.1126/science.1217447

Rafter, P. A., Sigman, D. M., & Mackey, K. R. M. (2017). Recycled iron fuels new production in the eastern equatorial Pacific Ocean. *Nature Communications*, *8*, 1100. https://doi.org/10.1038/s41467-017-01219-7

Rapp, I., Schlosser, C., Menzel Barraqueta, J. L., Wenzel, B., Lüdke, J., Scholten, J., et al. (2019). Controls on redox-sensitive trace metals in the Mauritanian oxygen minimum zone. *Biogeosciences*, *16*, 4157–4182. https://doi.org/10.5194/bg-16-4157-2019

Rapp, I., Schlosser, C., Rusiecka, D., Gledhill, M., & Achterberg, E. P. (2017). Automated preconcentration of Fe, Zn, Cu, Ni, Cd, Pb, Co, and Mn in seawater with analysis using high-resolution sector field inductively-coupled plasma mass spectrometry. *Analytica Chimica Acta*, *976*, 1–13. https://doi.org/10.1016/j.aca.2017.05.008

Rigby, S. J., Williams, R. G., Achterberg, E. P., & Tagliabue, A. (2020). Resource availability and entrainment are driven by offsets between nutriclines and winter mixed-layer depth. *Global Biogeochemical Cycles*, *34*, e2019GB006497. https://doi.org/10.1029/2019GB006497

Rolison, J. M., Middag, R., Stirling, C. H., Rijkenberg, M. J. A., & de Baar, H. J. W. (2015). Zonal distribution of dissolved aluminium in the Mediterranean Sea. *Marine Chemistry*, *177*, 87–100. https://doi.org/10.1016/j.marchem.2015.05.001

Rossby, T., Prater, M., Zhang, H., Lazarevich, P., & Pérez-Bunius, P. (1998). Isopycnal float studies of the subpolar front. *International WOCE Newsletter*, *32*, 32–35.

Rusiecka, D., Gledhill, M., Milne, A., Achterberg, E. P., Annett, A. L., Atkinson, S., et al. (2018). Anthropogenic signatures of lead in the Northeast Atlantic. *Geophysical Research Letters*, *45*, 2734–2743. https://doi.org/10.1002/2017GL076825

Ryan-Keogh, T. J., Macey, A. I., Nielsdóttir, M. C., Lucas, M. I., Steigenberger, S. S., Stinchcombe, M. C., et al. (2013). Spatial and temporal development of iron stress in relation to phytoplankton bloom dynamics in the high latitude North Atlantic. *Limnology and Oceanography*, *58*(2), 533–545. https://doi.org/10.4319/lo.2013.58.2.0533

Sanders, R., Brown, L., Henson, S., & Lucas, M. (2005). New production in the Irminger Basin during 2002. *Journal of Marine Systems*, *55*(3–4), 291–310. https://doi.org/10.1016/j.jmarsys.2004.09.002

Sarmiento, J. L., & Toggweiler, J. R. (1984). A new model for the role of the oceans in determining atmospheric PCO2. *Nature*, *308*(5960), 621–624. https://doi.org/10.1038/308621a0

Schlitzer, R., Anderson, R. F., Dodas, E. M., Lohan, M., Geibert, W., Tagliabue, A., et al. (2018). The GEOTRACES intermediate data product 2017. *Chemical Geology*, *493*, 210–223. https://doi.org/10.1016/j.chemgeo.2018.05.040

Schroller-Lomnitz, U., Hensen, C., Dale, A. W., Scholz, F., Clemens, D., Sommer, S., et al. (2019). Dissolved benthic phosphate, iron and carbon fluxes in the Mauritanian upwelling system and implications for ongoing deoxygenation. *Deep-Sea Research Part I: Oceanographic Research Papers*, *143*, 70–84. https://doi.org/10.1016/J.DSR.2018.11.008

Shelley, R. U., Landing, W. M., Ussher, S. J., Planquette, H., & Sarthou, G. (2018). Regional trends in the fractional solubility of Fe and other metals from North Atlantic aerosols (GEOTRACES cruises GA01 and GA03) following a two-stage leach. *Biogeosciences*, *15*(8), 2271–2288. https://doi.org/10.5194/bg-15-2271-2018

Sholkovitz, E. R., Sedwick, P. N., Church, T. M., Baker, A. R., & Powell, C. F. (2012). Fractional solubility of aerosol iron: Synthesis of a global-scale data set. *Geochimica et Cosmochimica Acta*, *89*, 173–189. https://doi.org/10.1016/j.gca.2012.04.022

St Laurent, L. C., & Thurnherr, A. M. (2007). Intense mixing of lower thermocline water on the crest of the Mid-Atlantic Ridge. *Nature*, *448*(7154), 680–683. https://doi.org/10.1038/nature06043

Sunda, W. G., Huntsman, S. A., & Harvey, G. R. (1983). Photoreduction of manganese oxides in seawater and its geochemical and biological implications. *Nature*, *301*(5897), 234–236. https://doi.org/10.1038/301234a0

Sutherland, D. A., Pickart, R. S., Peter Jones, E., Azetsu-Scott, K., Jane Eert, A., & Ólafsson, J. (2009). Freshwater composition of the waters off southeast Greenland and their link to the Arctic Ocean. *Journal of Geophysical Research*, *114*, C05020. https://doi.org/10.1029/2008JC004808

Tagliabue, A., Mtshali, T., Aumont, O., Bowie, A. R., Klunder, M. B., Roychoudhury, A. N., & Swart, S. (2012). A global compilation of dissolved iron measurements: Focus on distributions and processes in the Southern Ocean. *Biogeosciences*, *9*(6), 2333–2349. https://doi.org/10.5194/bg-9-2333-2012

Tagliabue, A., Sallee, J.-B., Bowie, A. R., Levy, M., Swart, S., & Boyd, P. W. (2014). Surface-water iron supplies in the Southern Ocean sustained by deep winter mixing. *Nature Geoscience*, *7*, 314–320.

Takano, S., Tanimizu, M., Hirata, T., & Sohrin, Y. (2014). Isotopic constraints on biogeochemical cycling of copper in the ocean. *Nature Communications*, *5*, 5663. https://doi.org/10.1038/ncomms6663

Tebo, B. M., Bargar, J. R., Clement, B. G., Dick, G. J., Murray, K. J., Parker, D., et al. (2004). Biogenic manganes oxides: Properties and mechanisms of formation. *Annual Review of Earth and Planetary Sciences*, *32*(1), 287–328. https://doi.org/10.1146/annurev.earth.32.101802.120213

Tomczak, M. (1999). Some historical, theoretical and applied aspects of quantitative water mass analysis. *Journal of Marine Research*, *57*(2), 275–303. https://doi.org/10.1357/002224099321618227

Twining, B. S., & Baines, S. B. (2013). The trace metal composition of marine phytoplankton. *Annual Review of Marine Science*, *5*(1), 191–215. https://doi.org/10.1146/annurev-marine-121211-172322

Twining, B. S., Rauschenberg, S., Morton, P. L., Ohnemus, D. C., & Lam, P. J. (2015). Comparison of particulate trace element concentrations in the North Atlantic Ocean as determined with discrete bottle sampling and in situ pumping. *Deep-Sea Research Part II: Topical Studies in Oceanography*, *116*, 273–282. https://doi.org/10.1016/J.DSR2.2014.11.005

Vink, S., & Measures, C. I. (2000). The role of dust deposition in determining surface water distributions of Al and Fe in the South West Atlantic. *Deep-Sea Research Part I: Oceanographic Research Papers*, *48*(13), 2787–2809.

Wedepohl, K. H. (1991). The composition of the upper earth's crust and the natural cycles of selected metals. In E. Merian (Ed.), *Metals and their compounds in the environment. Occurrence, analysis and biological relevance* (pp. 3–65). Weinheim: VCH.

Wu, J., & Boyle, E. A. (1997). Lead in the western North Atlantic Ocean: Completed response to leaded gasoline phaseout. *Geochemica Cosmochimica Acta*, *61*(15), 3279–3283. https://doi.org/10.1016/S0016-7037(97)89711-6

Wu, J., & Roshan, S. (2015). Cadmium in the North Atlantic: Implication for global cadmium–phosphorus relationship. *Deep-Sea Research Part II: Topical Studies in Oceanography*, *116*, 226–239. https://doi.org/10.1016/J.DSR2.2014.11.007

Wu, J., Roshan, S., & Chen, G. (2014). The distribution of dissolved manganese in the tropical–subtropical North Atlantic during US GEOTRACES 2010 and 2011 cruises. *Marine Chemistry*, *166*, 9–24. https://doi.org/10.1016/J.MARCHEM.2014.08.007

Wu, J., Sunda, W., Boyle, E. A., & Karl, D. M. (2000). Phosphate depletion in the Western North Atlantic Ocean. *Science*, *289*, 759–762. https://doi.org/10.1126/science.289.5480.759

Wyatt, N. J., Milne, A., Woodward, E. M. S., Rees, A. P., Browning, T. J., Bouman, H. A., et al. (2014). Biogeochemical cycling of dissolved zinc along the GEOTRACES South Atlantic transect GA10 at 40°S. *Global Biogeochemical Cycles*, *28*, 44–56. https://doi.org/10.1002/2013GB004637

Xie, R. C., Galer, S. J., Abouchami, W., Rijkenberg, M. J., de Jong, J., de Baar, H. J., & Andreae, M. O. (2015). The cadmium-phosphate relationship in the western South Atlantic: The importance of mode and intermediate waters on the global systematics. *Marine Chemistry*, *177*, 110–123. https://doi.org/10.1016/j.marchem.2015.06.011

Yamaguchi, R., & Suga, T. (2019). Trend and variability in global upper-ocean stratification since the 1960s. *Journal of Geophysical Research: Oceans*, *124*, 8933–8948. https://doi.org/10.1029/2019JC015439

Yamazaki, H., & Osborn, T. (1990). Dissipation estimates for stratified turbulence. *Journal of Geophysical Research*, *95*(C6), 9739–9744. https://doi.org/10.1029/JC095iC06p09739

Zurbrick, C. M., Boyle, E. A., Kayser, R. J., Reuer, M. K., Wu, J., Planquette, H., et al. (2018). Dissolved Pb and Pb isotopes in the North Atlantic from the GEOVIDE transect (GEOTRACES GA-01) and their decadal evolution. *Biogeosciences*, *15*(16), 4995–5014. https://doi.org/10.5194/bg-15-4995-2018